

Study of the hadronization of charged pions

Raphaël DUPRÉ

Institut de Physique Nucléaire, Orsay, France

Lamiaa EL FASSI

Mississippi State University, Mississippi State,

Mississippi 39762, USA

Kawtar HAFIDI

Physics Division, Argonne National Laboratory,

Argonne, Illinois 60439, USA

William BROOKS

Universidad Técnica Federico Santa María,

Valparaíso, Chile

January 4, 2017

Abstract

Hadronization is the process by which energetic quarks transform into colorless hadrons. The process is non-perturbative, therefore, only a qualitative understanding based on phenomenological models can be achieved. By comparing hadron production on different nuclei, one can measure the most sensitive variables to the hadronization phases, the transverse momentum broadening, that is believed to be tightly connected to the quark energy loss, and the multiplicity ratio, which is a measure of the hadron attenuation in the nuclear medium.

The goal of the experiment E-02-104 was the study of the quark propagation and hadronization dynamics using various nuclear targets. In this note, we focus on the production of two charged particles, positive and negative pions, to constrain theoretical models using a precise multidimensional analysis.

Contents

1	Introduction	3
1.1	Kinematic Variables and Observables	4
1.2	Theoretical Efforts	5
1.3	Previous Measurements	6
2	Data Analysis	9
2.1	Introduction	9
2.2	Particle Identification	10
2.2.1	Electron Identification	10
2.2.2	π^- Identification	13
2.2.3	π^+ Identification	15
2.2.4	Target Determination	16
2.2.5	Data Quality	18
2.3	Extraction of Multiplicity Ratio and ΔP_{\perp}^2	19
2.3.1	Method	19
2.3.2	Preliminary Results	20
2.4	Corrections	20
2.4.1	Acceptance Correction	20
2.4.2	Coulomb Correction	28
2.4.3	Radiative Correction	28
2.4.4	Isospin Correction	31
2.5	Systematic Uncertainties	32
2.5.1	Quality of the Detection	33
2.5.2	Target Reconstruction	33
2.5.3	Acceptance	34
2.5.4	Total Systematic Budget	35
3	Results and Discussions	36
3.1	Multiplicity Ratio	36
3.1.1	A Dependence	36
3.1.2	Cronin Effect	36
3.1.3	ν Dependence	38
3.1.4	z Dependence	40
3.1.5	Q^2 Dependence	41
3.2	Transverse Momentum Broadening	41
3.2.1	A Dependence	41
3.2.2	Q^2 Dependence	42

1 Introduction

The hadronization process by which partons fragment into hadrons is experimentally well studied, and the associated fragmentation functions are extracted from the fit of experimental data over a wide range of kinematics [1]. Nevertheless, the hadron formation is a non perturbative process, which can not be described theoretically, but only via a systematic study of the whole hadronization mechanism (see figure 1) for energies above the resonance region. In Deep Inelastic Scattering (DIS), the virtual photon interacts with a quark which propagates quasi-free emitting gluons during the so-called production time. After neutralizing its color, the quark becomes a pre-hadron that eventually evolves to a full hadron after the formation time. The advantage of using nuclear targets is that the hadronization process occurs, at least partially, inside the nuclear matter, which allows the extraction of hadronization time-scales by comparing different behavior of quarks and colorless pre-hadrons in the medium. The measurement of pions production is especially suited for this analysis because they are easy to detect and abundant in the nuclear deep inelastic scattering (nDIS).

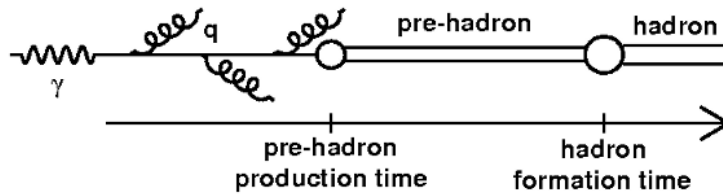


Figure 1: Sketch of the hadronization process.

The hadronization in nuclear matter is a key process of the Quantum Chromo-Dynamics theory (QCD) because it leads to major theoretical uncertainties in numerous measurements. As the nuclear medium is hot and evolving in Relativistic Heavy Ion Collisions (RHIC), DIS experiments at JLab energies are well suited to test different theoretical models, including the RHIC's ones, because the size of cold nuclei is stable and known. A quantitative understanding of the hadronization process in nuclei is also an interesting theme for neutrino experiments that often use nuclei to maximize their cross sections. The hadronization can give an important information about nuclei through the quark energy loss, for example, Arleo's model [2] correlates the quark energy loss with a gluon density, and Kopeliovich et al.'s model [3] correlates the $\Delta\langle P_T^2 \rangle$ with the saturation scale. Other models [4] utilize different assumptions to describe the pre-hadron evolution into a full hadron. Therefore, high precision measurements are very important to discriminate between different models.

In order to constrain the existing models we extracted our results using a tight multi-dimensional binning. That was viable due to the high statistics of our EG2

data, which allowed the study of both pions production over a wide kinematic range.

We present in section 1.2 a highlight of different models' families describing the hadronization process in hot and cold nuclear matter, then in section 1.3 we make a rapid overview of published results. For more detailed information, we refer the readers to the review of Accardi *et al.* [5].

1.1 Kinematic Variables and Observables

In this analysis we use the following Semi-Inclusive Deep Inelastic Scattering (SIDIS) variables:

- $\nu = E_i - E_f$ is the energy transferred by the lepton probe in the laboratory frame, where E_i is the beam energy and E_f is the scattered electron energy,
- $Q^2 = 4E_i E_f \sin^2(\theta_e/2)$ is the 4-momentum transferred, with θ_e is the polar angle of a scattered electron,
- $x_{Bj} = \frac{Q^2}{2M_n \nu}$ is the proton momentum fraction carried by the struck quark, with M_n is the nucleon mass,
- $W^2 = M_n^2 - Q^2 + 2M_n \nu$ is the mass squared of the hadronic final state,
- $z_h = E_h/\nu$ is the virtual photon energy fraction carried by the measured hadron, with E_h is the hadron energy,
- P_T^2 is the hadron transverse momentum measured with regard to the virtual photon direction,
- ϕ_h is the angle between the leptonic plane (containing initial and scattered electrons) and the hadronic plane (containing the virtual photon and a measured hadron),
- $x_F = P_L/P_L^{max}$ is the longitudinal momentum fraction carried by the hadron, and calculated with respect to the virtual photon direction in the laboratory frame.

We define the multiplicity ratio as:

$$R_A^h(Q^2, \nu, z_h, P_T^2) = \frac{N_A^h(Q^2, \nu, z_h, P_T^2)/N_A^e(Q^2, \nu)}{N_D^h(Q^2, \nu, z_h, P_T^2)/N_D^e(Q^2, \nu)}, \quad (1)$$

N_A^e and N_A^h are the number of electrons and semi-inclusive hadrons h measured simultaneously on a target A . The multiplicity ratio represents the attenuation of the hadron h in a nuclear target A .

We define the transverse momentum broadening as:

$$\Delta\langle P_T^2 \rangle = \langle P_T^2 \rangle_A - \langle P_T^2 \rangle_D, \quad (2)$$

where $\langle P_T^2 \rangle_A$ is the mean transverse momentum measured on a target A .

1.2 Theoretical Efforts

The different models explaining the data can be separated in three families; some assume that the quark loses energy in the medium and that either the hadronization occurs outside the medium or the hadronic interaction is negligible, others neglect the quark energy loss and consider only the hadron and pre-hadron absorption, and the third category considers both interactions. For illustration, we will give an example of each case, but for more detailed information, we refer the readers again to our reference [5], which is more exhaustive and highlights also models describing RHIC's experiments.

In [6], E. Wang and X.-N. Wang, described HERMES data using only the parton energy loss, hence the observed suppression is due to the fact that a lower energy quark fragments into a low number of hadrons at a very low z . This kind of models is suitable for both RHIC and nDIS experiments since it permits a common interpretation of hadron suppression in the nuclear matter. Moreover, various calculations have described the parton energy loss in the nuclear medium using the \hat{q} ($\text{GeV}^2 \text{ fm}^{-1}$) parameter, that is defined as the quark transverse momentum normalized by its propagation path length. In these models, \hat{q} is mainly related to the P_T broadening observable. The main difficulty of quark energy loss models is the lack of a coherent description for both multiplicity ratios and P_T broadening behaviors. Recent models used a \hat{q} to reproduce multiplicity ratio, which is too large to describe the transverse momentum broadening.

The other transport model, GiBUU [4], is based on the Boltzmann equation that employs hadronic and pre-hadronic interactions in the nuclear matter without involving any quark energy loss. This model reproduces very well most of hadrons' multiplicity ratios, however, it failed to describe the transverse momentum broadening.

Furthermore, B.Z. Kopeliovich et al. [7] described the process by neither neglecting the quark energy loss nor the hadron absorption, but used both $\Delta\langle P_T^2 \rangle$ and R_A^h observables to differentiate between these effects. In that case, the transverse momentum broadening is correlated with the quark energy loss, and the suppression of multiplicity ratios is explained by the hadron absorption in the nuclear medium.

To conclude it is important to point out that no consensus is reached on which mechanisms are dominant. It is, therefore, important to perform precise measurements with the appropriate observables to disentangle these effects.

1.3 Previous Measurements

Hadron multiplicity ratios in nuclei were measured in numerous lepton facilities: L.S. Osborne *et al.* [8] at SLAC, L. Hand *et al.* [9], the E665 collaboration [10] at FNAL, and the European Muon Collaboration [11, 12] at CERN. These measurements revealed the main features of the hadronization mechanism in nuclei by showing a suppression of hadrons' production in heavy nuclei. This suppression appears to be reduced at higher ν and lower z , and it can even inverse sign and become an increased yield at very low z .

Figures 2, 3 and 4 show a sample of the most recent HERMES data [13], where numerous hadrons were individually studied, and new variables linked with the transverse momentum were used in addition to the usual multiplicity ratio.

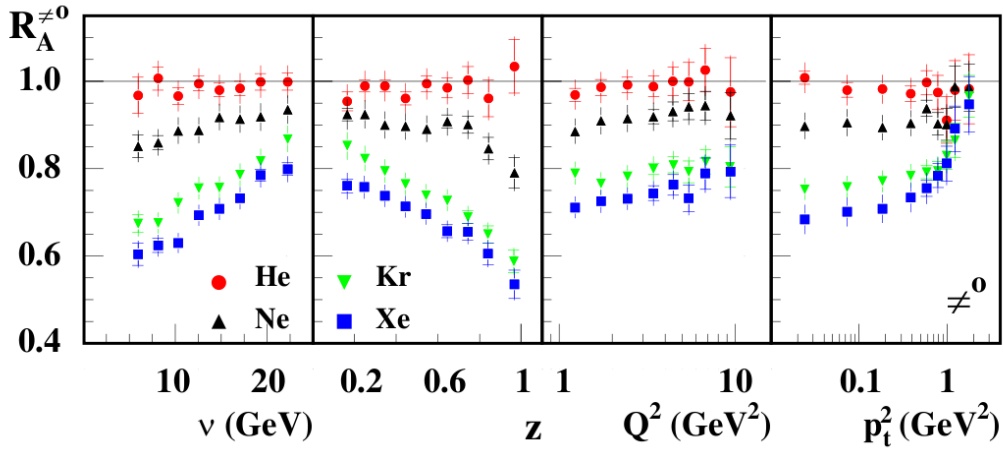


Figure 2: Multiplicity ratios of π^0 as a function of various kinematical variables from the HERMES collaboration [14]

The good precision of HERMES data shed light on new hadronization features, such as the behavior of K^+ s, which have less attenuation than pions (see figure 2) but an excess on $\Delta\langle P_T^2 \rangle$. Must note that it is difficult to reproduce this behavior on models where only one hadronization stage is taken into account to explain all effects. Likewise, the different behavior of protons compared to anti-protons (see figure 3) is interesting and needs more precise analyses to unravel it since most of the existing models do not treat yet the baryons' hadronization.

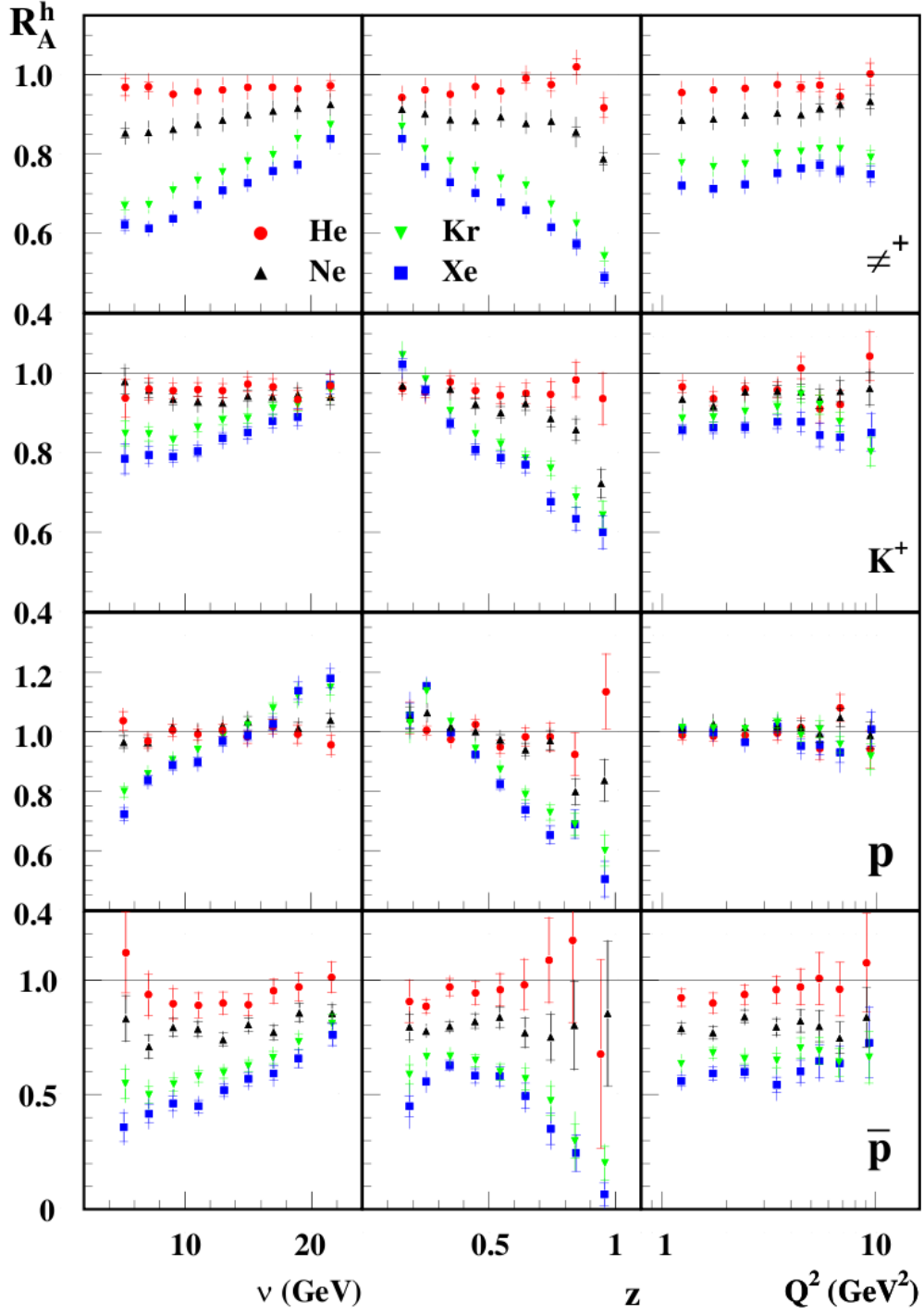


Figure 3: Multiplicity ratios of π^+ , K^+ , protons and anti-protons as a function of various kinematical variables from the HERMES collaboration [13]

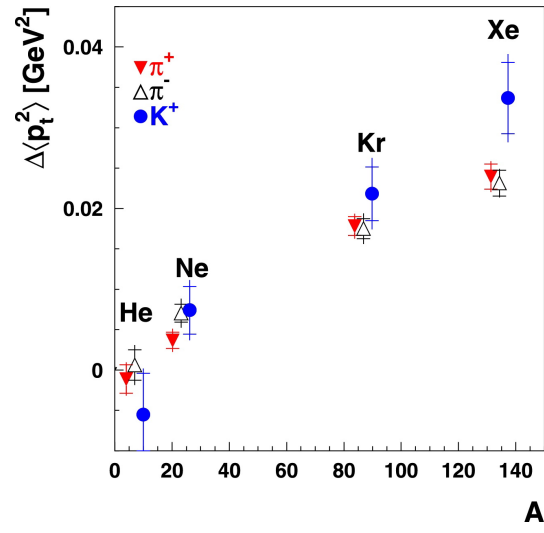


Figure 4: Transverse momentum broadening for various particles from the HERMES collaboration [15]

2 Data Analysis

2.1 Introduction

This chapter treats the analysis of CLAS data taken for both experiments E-02-104 [16] and E-02-110 [17]. The run period, named *eg2*, was composed of three phases labeled *a*, *b* and *c*. The analysis is performed on the data collected in the beginning of 2004 during the third phase (*eg2c*), for which the beam energy was 5.014 GeV¹.

As the two married experiments aimed at comparing deuterium with heavy nuclei, it was decided to use a double target system [18]. The first target was filled with a liquid deuterium, and the second was a solid target. The latter was made of either carbon, aluminum, iron, tin or lead, and was changed remotely (see figure 5). The two targets were separated by only 4 cm in order to minimize the difference on CLAS acceptance between them. The advantage of having two targets mounted simultaneously on the beam line is that several systematic effects related to the beam and detector's properties will cancel in the nuclear ratio.



Figure 5: Picture of the *eg2* target system. The cryogenic target is in the back wrapped with aluminum foils, while solid targets are held by mechanical arms that were controlled remotely. In the picture, the top solid target is in the beam line.

The analysis of the experiment E-02-110, focusing on the study of color transparency effects, has been approved and published [19]. As this analysis went through a careful review by the CLAS collaboration, we have adapted similar analysis methods as much as possible. In particular, the electron selection presented here is very similar to theirs; the main difference being a new target determination method. The pion

¹The other phases of the run gave only small amounts of data at beam energies of 4 and 4.7 GeV. Thus, we decided to not use them in this analysis.

identification cuts are, however, tightened in this analysis as we have less constraints on the kinematics to exclude any possible pions' contamination.

In the section 2.2, we identify the following particles, e^- , π^- and π^+ using a series of cuts on various detector outputs. For pions, we require a positive status of drift chambers (DC) and scintillator counters (SC) local signals, in addition to the global status reconstructed with the time-based tracking correction. For electron identification, we use good signals from all detectors, DC, Cherenkov Counters (CC), SC and the Electromagnetic Calorimeter (EC).

Once all particles are identified, we extract our two observables, multiplicity ratios and the transverse momentum broadening. Their derivation method is presented in the section 2.3, while a list of our corrections is summarized in the section 2.4. The budget of our systematical uncertainties is detailed in the section 2.5, and the final analysis results are presented and discussed in the next chapter.

2.2 Particle Identification

2.2.1 Electron Identification

First, we apply a fiducial cut on the EC local coordinates to remove electrons detected close to the calorimeter's edges ($U_{EC} > 40$ cm, $V_{EC} < 360$ cm and $W_{EC} < 395$ cm). These hits are problematic because part of the electromagnetic shower might be generated outside of the detector. That leads to a wrong measurement of the energy deposited.

To reject pions, we apply a momentum-dependent cut of the energy deposited in the inner (E_{in}) and the outer parts (E_{out}) of the calorimeter as,

$$\mu \left[1 - \frac{0.3}{\sqrt{a}} \right] - \frac{E_{in}}{p} \leq \frac{E_{out}}{p} \leq \mu \left[1 + \frac{0.3}{\sqrt{b}} \right] - \frac{E_{in}}{p}, \quad (3)$$

where $\mu = 0.271$ is the mean of the total energy fraction deposited in the calorimeter, the parameter a is set to 0.5, and the parameter b varies with momenta, as shown in table 1. The derivation of b was motivated by the non-linear momentum dependence of the energy deposited on both EC regions (see figure 6). As pions are minimum ionizing particles, they are expected to lose a constant energy in the inner part of the calorimeter (around 30 MeV), regardless of their momenta. Therefore, by requesting more than 60 MeV to be deposited, we efficiently cut the pion contamination (see figure 7).

In the CC, the mean number of photo-electrons² from a high energy electron is expected to be around 10. However, hadrons can generate noise due to δ electrons produced in the materials of the detector. This signal is expected to be around one to

²Photo-electrons are electrons produced in the front window of the Photo-Multiplier Tube (PMT) by a single photon.

Momentum bin (GeV/c)	Parameter b
0.5 - 0.7	0.85
0.7 - 0.9	0.8
0.9 - 1.1	0.85
1.1 - 1.3	1.05
1.3 - 1.5	1.1
1.5 - 1.7	1.35
1.7 - 1.9	1.35
1.9 - 2.1	1.45
2.1 - 2.3	1.35
2.3 - 2.5	1.35
2.5 - 2.7	1.35
2.7 - 2.9	1.3
2.9 - 3.1	1.35
3.1 - 3.3	1.35
3.3 - 3.5	1.5
3.5 - 3.7	1.6
3.7 - 3.9	1.8
3.9 - 4.1	1.8
4.1 - 4.3	1.8
4.3 - 4.5	1.8

Table 1: Values of the parameter b used in equation 3 for different momentum ranges [19].

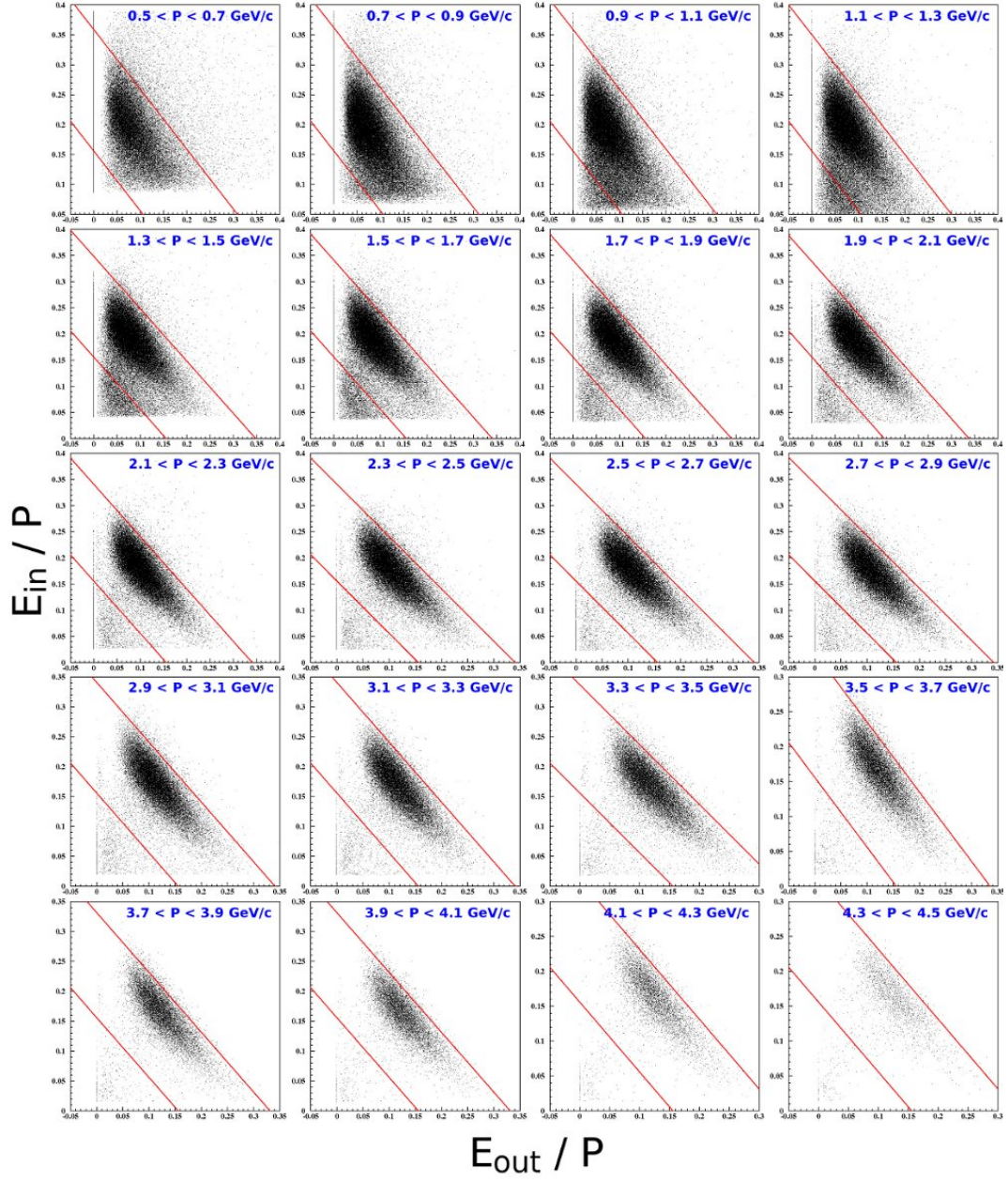


Figure 6: Energy deposited in the inner part of the EC (E_{in}) as a function of the energy deposited in its outer part (E_{out}) normalized by tracks' momenta. Each panel is for a different momentum range, and the drawn red lines illustrate the cuts from equation 3.

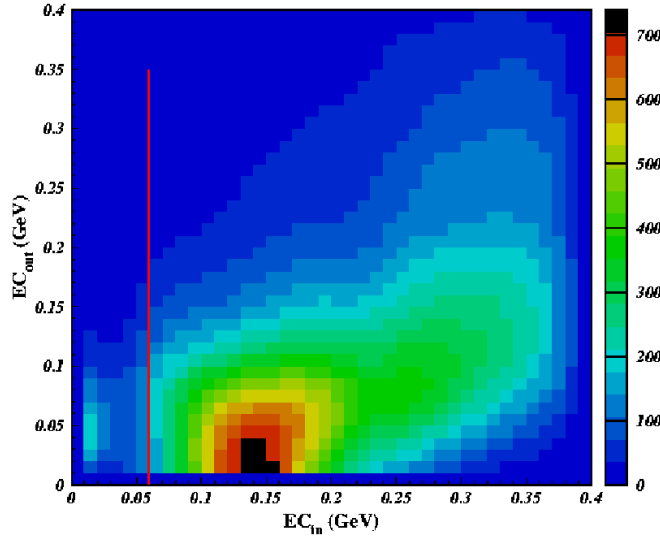


Figure 7: Energy deposited in the inner part of the EC as a function of the energy deposited in its outer part. The red line illustrates the applied cut.

two photo-electrons. Hence, to get rid of δ -electrons, we kept only tracks with more than 2.5 photo-electrons, as depicted in figure 8.

To select electrons, we also require that particles are negatively charged³. Positively charged particles verifying electrons' cuts are identified as positrons. In the rest of this analysis, we used only events with a single electron and no positron to avoid any confusion between the scattered electron and electrons originating from hadronic decays or a photon conversion.

2.2.2 π^- Identification

To identify negatively charged pions, we select negative tracks which didn't verify electrons' identification cuts. Pions are detected in the angular range from ~ 10 to ~ 140 degrees using only DC and SC signals.

This identification consists mostly of a time of flight (TOF) test. We define the relativistic particles' velocity difference as $\Delta\beta = \beta_{measured} - \frac{p}{\sqrt{p^2 + m_\pi^2}}$, which is required to be zero within ± 0.03 . Figure 9 illustrates the effect of this cut. As we noticed there are not much negative kaons or anti-protons, we concluded that their contamination must be small (see section 2.5.1 for more detailed study).

In principle, a pion identification could be improved using the Cherenkov counter for momenta higher than 2.5 GeV/c. But, the observed low CC efficiency (see figure

³In the CLAS reconstruction software, the electric charge is determined based on the tracks' bending direction in drift chambers.

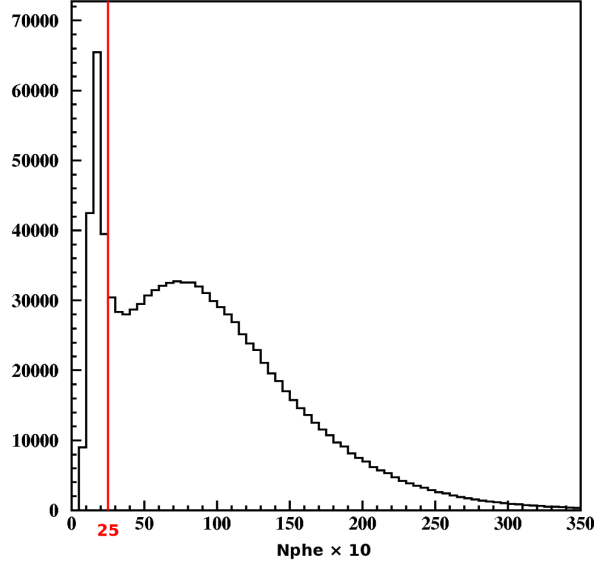


Figure 8: Number of photo-electrons ($\times 10$) per tracks. The red line shows the applied cut to remove any low-energy pions' contamination.

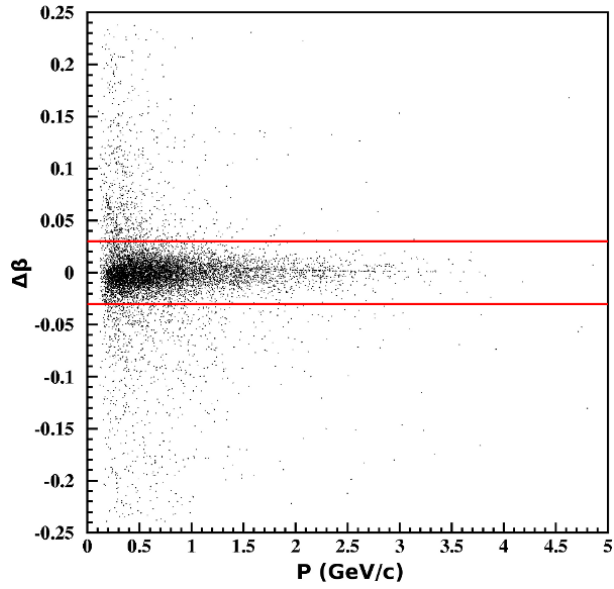


Figure 9: $\Delta\beta$ of negatively charged particles as a function of momentum (GeV/c). The red lines shows the applied cuts to select negative pions.

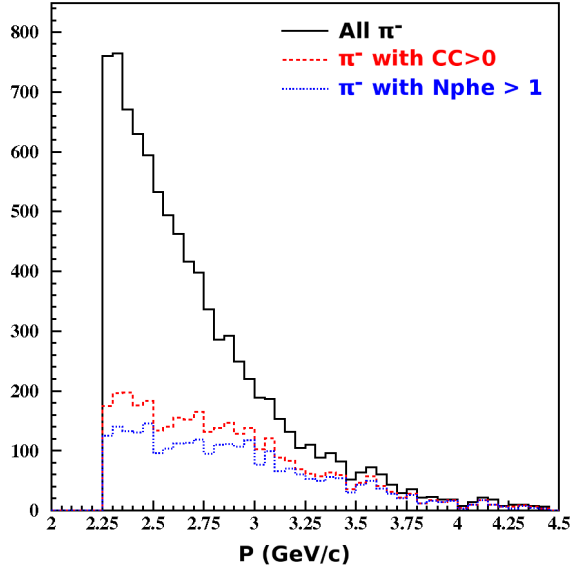


Figure 10: Histograms of momentum (GeV/c) for π^- s. The black, red, and blue distributions are, respectively, for all identified π^- s, pions that fire Cherenkov counters, and pions that fire CC with more than one photo-electron.

10) especially at momenta close to the CC threshold ($\sim 25\%$ at 2.5 GeV/c and $\sim 50\%$ at 3 GeV/c) makes its use less compelling. Moreover, as only a very small amount of K^- s and no \bar{p} s are present on figure 9, we decided to not use CC on this pions' identification.

2.2.3 π^+ Identification

The identification of positively charged pions is similar to that of negative pions. However, the time of flight plot is significantly more busy (see figure 11), indicating a significant contamination from K^+ s and protons at a higher momentum. As the CC is not efficient enough for a hadron separation, the numerous kaons and protons should be removed by the following tighter TOF cuts:

$$p_\pi \leq 3.375 \text{ GeV/c} : \quad \Delta\beta > \max \left(-0.03, \frac{p}{\sqrt{p^2 + 0.4^2}} \right), \quad (4a)$$

$$p_\pi > 3.375 \text{ GeV/c} : \quad \Delta\beta > \max \left(-0.02, \frac{p}{\sqrt{p^2 + 0.7^2}} \right). \quad (4b)$$

These cuts permit to minimize the kaon contamination, below 2.5 GeV/c, and

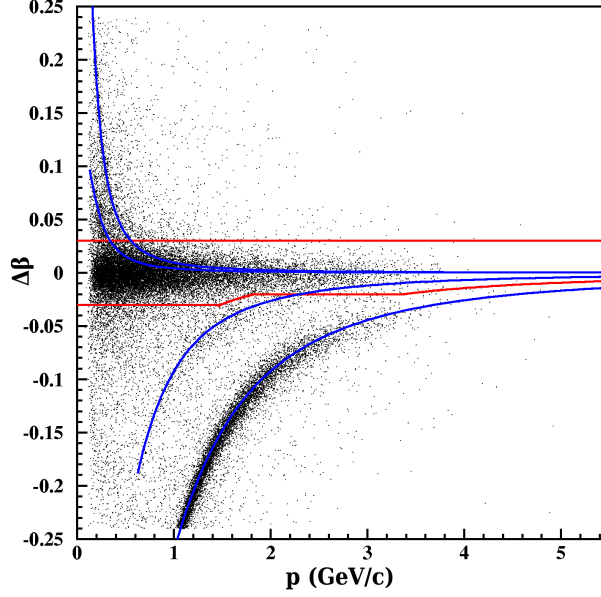


Figure 11: $\Delta\beta$ of positively charged particles as a function of momentum (GeV/c). The red lines show the applied cuts to select positive pions. The blue lines indicate other particles' theoretical positions, and present from top to bottom positrons, muons, kaons and protons.

the proton contamination for all momenta. The kaon contribution cannot be avoided, however, it should remain small ($\sim 3\%$ according to simulation) with only a small effect on our final results (see section 2.5.1 for more details). Because protons could lead to even more contamination than kaons, a stricter cut is used at a high momentum. This cut is also justified by HERMES data [13], which showed a very different behavior of protons compared to other hadrons.

2.2.4 Target Determination

To differentiate between the two targets and remove the background, we need to determine the origin of our final-state particles. As illustrated in figure 12, the small misalignment of the beam with the CLAS detector led to an artificial shift on different sectors' z-vertex positions. To correct from this effect, we added the shift shown in table 2 when determining each particle's vertex position. Those values were obtained from the fit of the solid target distribution on each sector.

The position of our targets could also vary from a run to another, but this did not happen too often in this experiment. Indeed, except for aluminum, other targets remained in the same position within one or two millimeters. All targets' positions, in CLAS coordinates, are given in table 3.

The detected electrons are associated with the solid target if their vertex position

Sector	Shift (cm)
1	+ 0.1
2	- 0.4
3	- 0.6
4	- 0.1
5	+ 0.4
6	+ 0.6

Table 2: Values used to correct the vertex position on each sector

Target	Carbon	Al (1)	Al (2)	Iron	Tin	Lead
Liquid	-30.1	n/a	n/a	-30.2	-30.1	-30.1
Solid	-24.7	-25.0	-23.8	-24.9	-23.8	-24.9

Table 3: The measured mean vertex position of our nuclear targets relative to the center of CLAS (in cm). Must note that aluminum data are separated in two sets because this target's position has brutally changed. Moreover, during these runs the deuterium target was empty.

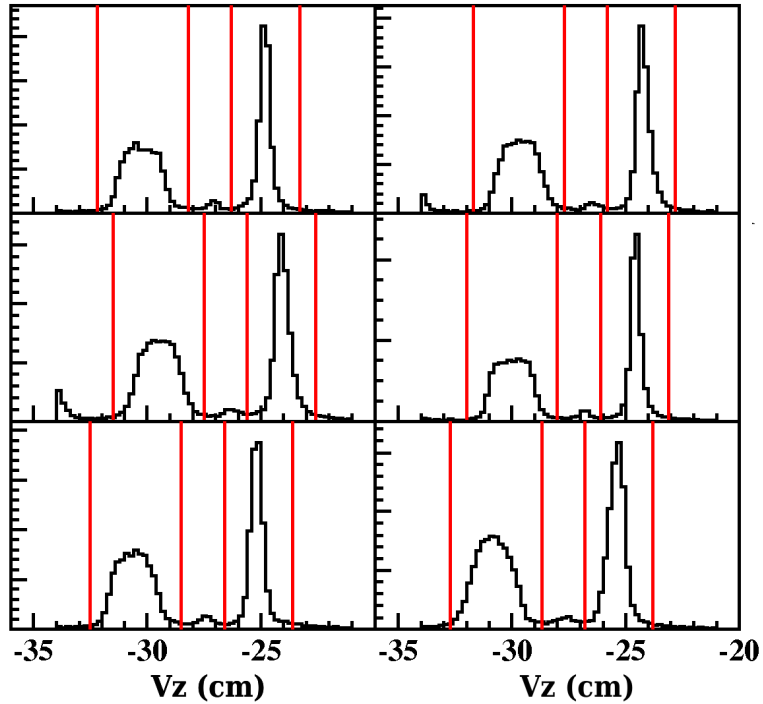


Figure 12: Sector-by-sector electrons' vertex distributions. The latter are reconstructed along the beam direction and relative to the center of CLAS located at 0 cm. The red lines show the applied cuts to select the two targets.

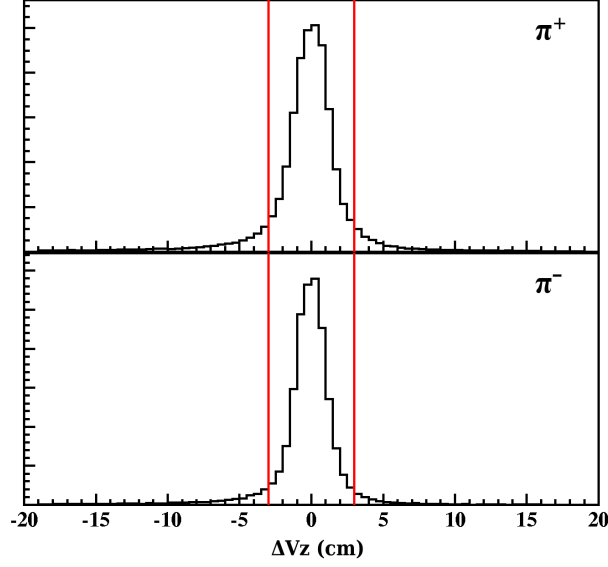


Figure 13: The difference between electrons and pions z-vertex positions. π^+ s and π^- are plotted, respectively, in the top and bottom panels. The red lines show the applied cuts to select both pions.

is less than 1.5 cm ($\sim 3 \sigma$) from the values shown on table 3. For the liquid target, the cut is a bit larger, 2 cm, in order to count for the cryogenic target's size (see figure 12). The pions' vertex was checked against the electron one and was imposed to satisfy this additional condition $|Vz^{e^-} - Vz^\pi| < 3$ cm (see figure 13).

2.2.5 Data Quality

To check the quality of the runs⁴, we monitored the ratio of scattered electrons yields obtained from solid and liquid targets. In case of the beam hitting other materials in the beam-line or any detector is not working properly, this ratio will be off and indicates problematic runs. A figure 14 shows electrons yields' ratios for different nuclear target; we fitted these ratios to extract the mean value for each target, then we discarded runs that were 5σ away from the appropriate mean. Must note that these ratios were consistent with our target's thicknesses given in [18] except for a carbon target. For that reason, the density of the latter was recently remeasured, and its new value was finally matching our data⁵.

⁴Runs were formed roughly from two hours of data, but they were much smaller in case of problems.

⁵i.e. $(1.747 \pm 0.0007) \text{ g/cm}^3$ instead of 2.235 g/cm^3

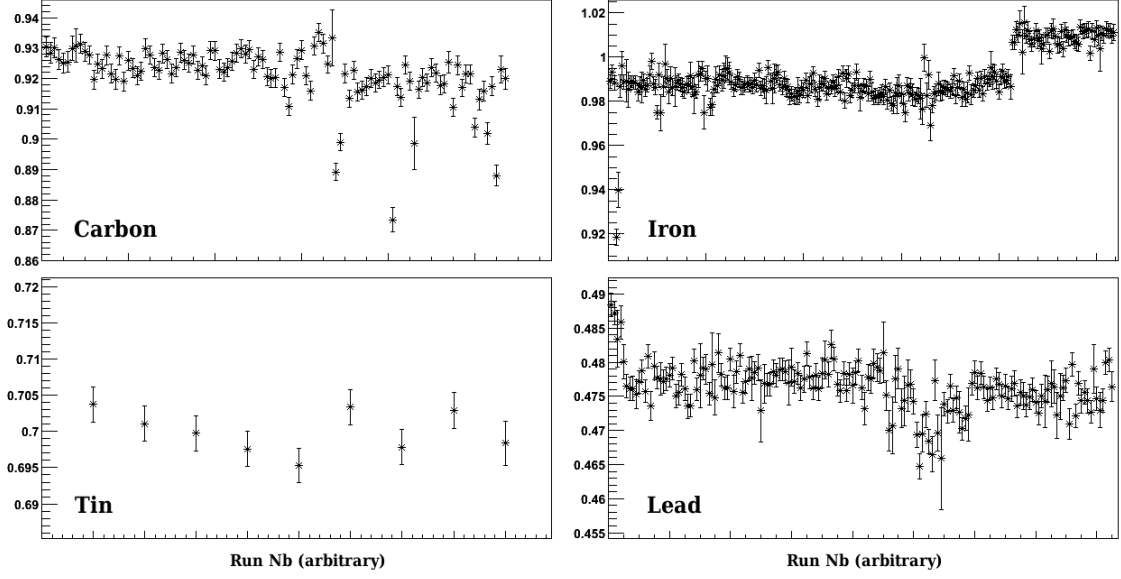


Figure 14: Ratio of scattered electrons yields (solid over deuterium) for each run.

2.3 Extraction of Multiplicity Ratio and ΔP_{\perp}^2

Since we are interested in deep inelastic scattering, we use the following cuts: $Q^2 > 1 \text{ GeV}^2/c^2$ and $W > 2 \text{ GeV}$. We also apply a cut on the energy transferred fraction, $y = \nu/E_{beam} < 0.85$. This cut aims to remove the low energy electrons that are significantly affected by radiative effects and sat at the limit of our trigger threshold.

2.3.1 Method

Once the identification is done, the calculation of our two observables and their statistical uncertainties is straightforward. The latter are given by:

$$\frac{\delta(R_A^h)}{R_A^h} = \sqrt{1/N_A^h + 1/N_A^e + 1/N_D^h + 1/N_D^e} \quad (5)$$

and

$$(\delta(\Delta\langle P_{\perp}^2 \rangle))^2 = (\langle P_{\perp}^4 \rangle - \langle P_{\perp}^2 \rangle^2)_A / N_A^h + (\langle P_{\perp}^4 \rangle - \langle P_{\perp}^2 \rangle^2)_D / N_D^h. \quad (6)$$

However, the implementation of acceptance and radiative corrections is done through some given weights to each event based on its kinematics. The multiplicity ratio then becomes

$$R_A^h(Q^2, \nu, z_h, P_{\perp}^2) = \frac{\sum \omega_A^h(Q^2, \nu, z_h, P_{\perp}^2) / \sum \omega_A^e(Q^2, \nu)}{\sum \omega_D^h(Q^2, \nu, z_h, P_{\perp}^2) / \sum \omega_D^e(Q^2, \nu)}, \quad (7)$$

where ω is the weight associated with the event, and the sums run over all measured

particles. The expression of the transverse momentum broadening remains as

$$\Delta\langle P_{\perp}^2 \rangle = \langle P_{\perp}^2 \rangle_A - \langle P_{\perp}^2 \rangle_D, \quad (8)$$

but with

$$\langle P_{\perp}^2 \rangle = \frac{\sum (P_{\perp}^2 \times \omega(Q^2, \nu, z_h, P_{\perp}^2))}{\sum \omega(Q^2, \nu, z_h, P_{\perp}^2)}. \quad (9)$$

Thus, new expressions of the weighted statistical uncertainties are:

$$\frac{\delta(R_A^h)}{R_A^h} = \sqrt{\left(\frac{\sum \omega_A^{h^2}}{(\sum \omega_A^h)^2}\right) + \left(\frac{\sum \omega_A^{e^2}}{(\sum \omega_A^e)^2}\right) + \left(\frac{\sum \omega_D^{h^2}}{(\sum \omega_D^h)^2}\right) + \left(\frac{\sum \omega_D^{e^2}}{(\sum \omega_D^e)^2}\right)} \quad (10)$$

and

$$\begin{aligned} (\delta(\Delta\langle P_{\perp}^2 \rangle))^2 &= \left(\frac{\sum \omega_A^h P_{\perp}^4}{\sum \omega_A^h} - \left(\frac{\sum \omega_A^h P_{\perp}^2}{\sum \omega_A^h}\right)^2\right) \times \left(\frac{\sum (\omega_A^h)^2}{(\sum \omega_A^h)^2}\right) \\ &+ \left(\frac{\sum \omega_D^h P_{\perp}^4}{\sum \omega_D^h} - \left(\frac{\sum \omega_D^h P_{\perp}^2}{\sum \omega_D^h}\right)^2\right) \times \left(\frac{\sum (\omega_D^h)^2}{(\sum \omega_D^h)^2}\right). \end{aligned} \quad (11)$$

2.3.2 Preliminary Results

To provide some insight into the quality of our data, we present in figure 15 few preliminary results before the application of any corrections. These preliminary results will be used also to illustrate the effects of the corrections discussed below.

2.4 Corrections

2.4.1 Acceptance Correction

The acceptance correction consists of applying weights to the experimental data event by event to correct for any detection inefficiencies of used detectors. Incidentally, it also corrects for other small detection issues, such as misidentification and re-scattering on detectors' materials. The quality of the correction depends on the ability of the simulation to reproduce the experiment, the accumulated statistics, and the size of interfering effects, such as the bin migration. For this correction, we applied the method from the approved and published analysis from the same eg2 data [19].

Simulation To correct for acceptance effects, we simulated a total of 100 million events per target (^2H , C, Fe and Pb) using the PYTHIA [20] event generator that

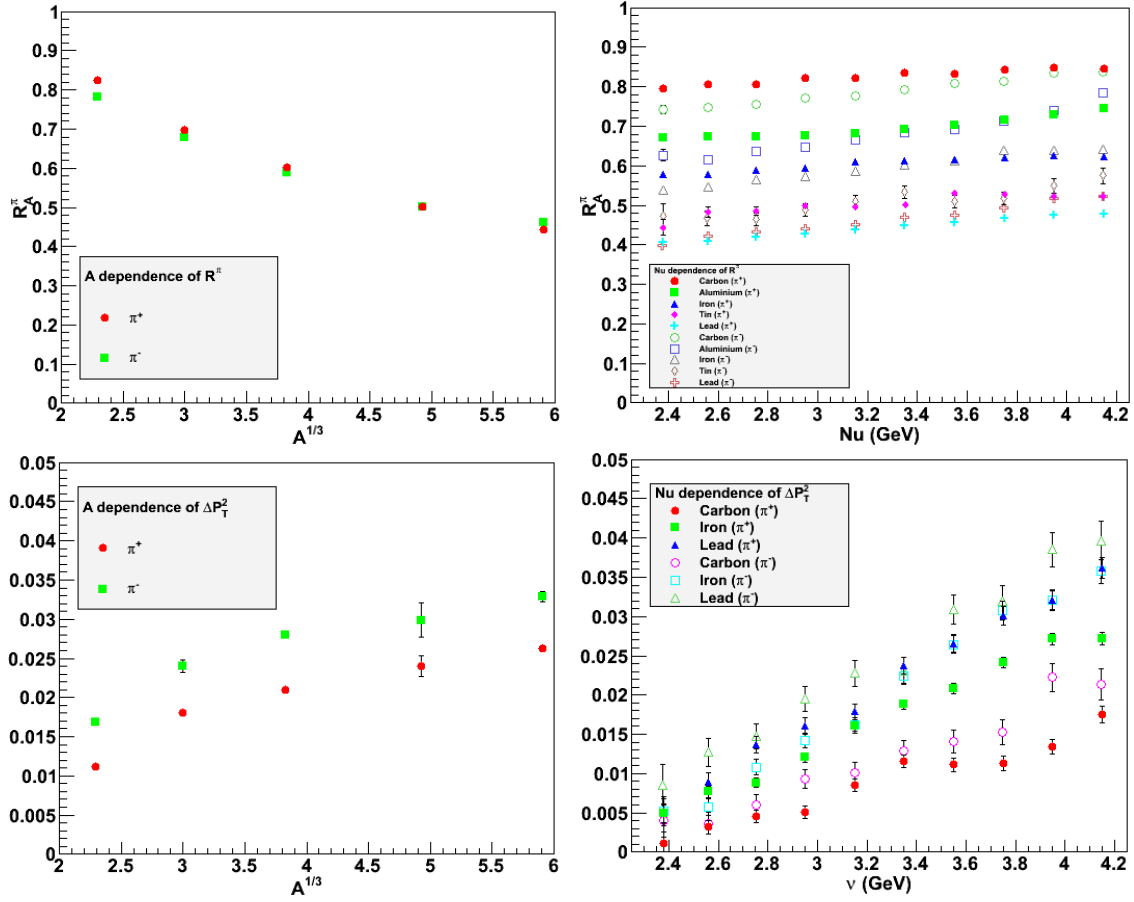


Figure 15: Results for multiplicity ratios (top) and the transverse momentum broadening (bottom) before applying any corrections.

was slightly modified to include Fermi motion effects. The generated events are processed by CLAS softwares (GSIM, GPP and user.ana) to simulate the detector and the reconstruction process similarly to the experimental data.

Then the simulated data are processed in a similar way than the experimental data by applying the cuts described in the section 2.2. Overall the simulation reproduces quite well the detectors responses, yet two issues might affect us and have to be understood. First, the efficiency of the CC is overestimated in the simulation. On the electron side the signal is a little stronger in the simulation (11 photo-electrons) compared to experimental data (8 photo-electrons), but this feature should not affect us too much, because we are cutting only the tail of the distribution in both cases. Second, since in the simulation the beam is perfectly aligned with CLAS, the vertex cuts do not need to be shifted from one sector to an other. Therefore, we do not apply the shift from table 2 to the simulated data; the resulting cuts are shown in figure 16.

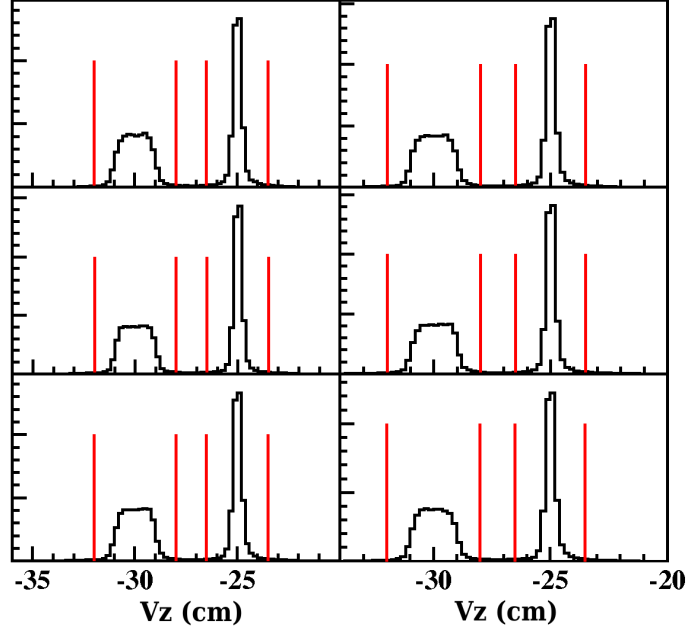


Figure 16: Sector by sector electrons' vertex distributions from the **simulated data**. The latter are reconstructed along the beam direction, and relative to the CLAS center. The red lines show the used cuts to select both targets.

The kinematical distributions from the simulation are compared to the experimental ones. This is important for the acceptance correction, to see whether or not, we can integrate over any variables in this correction. Comparisons between simulated and experimental data are shown in figures 17 to 20. The agreement is reasonable, but not perfect. The differences are due to the PYTHIA simulation, which is not including some physical effects, such as radiative and diffractive processes.

Correction of the Data The acceptance correction coefficients are defined as the ratio of reconstructed and generated events,

$$\text{Acc} = \frac{N_{rec}}{N_{gen}}. \quad (12)$$

Experimental data were corrected using the weights defined as $\omega = 1/\text{Acc}$. These coefficients are calculated in many bins, in order to be independent of the imperfections of our event generator. However, an excess of bins could lead to a strong bin migration⁶, which might introduce a bias in case it becomes quite large.

We used a 4-dimensional binning to divide the large phase space of our two particles' final state. However, to evaluate the associated systematic errors with this correction,

⁶Fraction of events not reconstructed in the bin they were produced in.

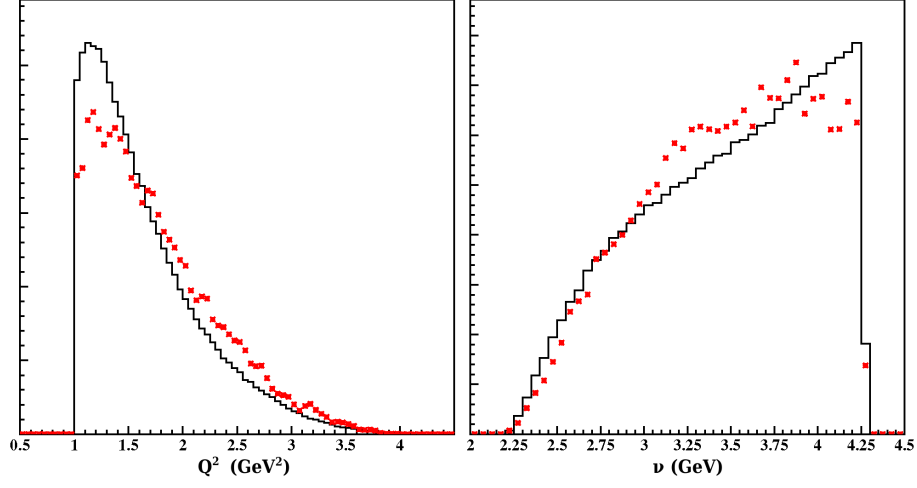


Figure 17: Comparisons, for Q^2 (GeV²/c²) and ν (GeV), of the distributions from simulated (red crosses) and experimental (histogram) data using deuterium target.

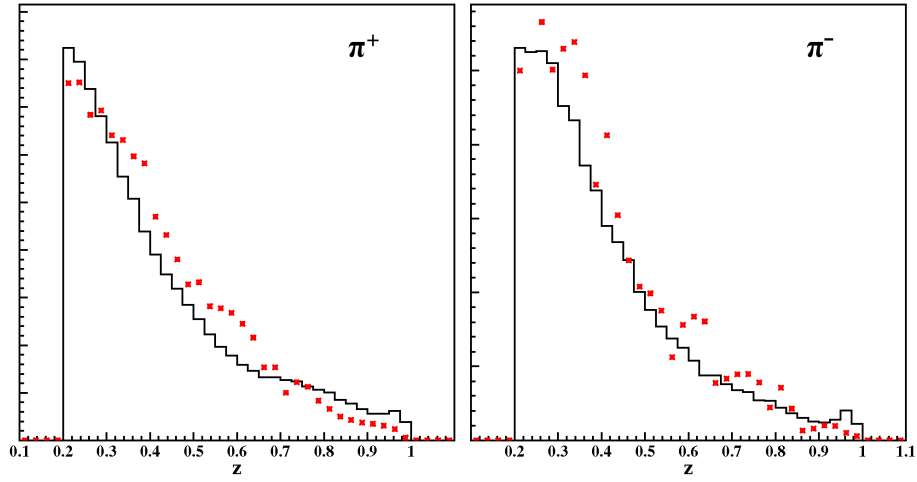


Figure 18: Comparisons, for z of charged pions, of the distributions from simulated (red crosses) and experimental (histogram) data using deuterium target.

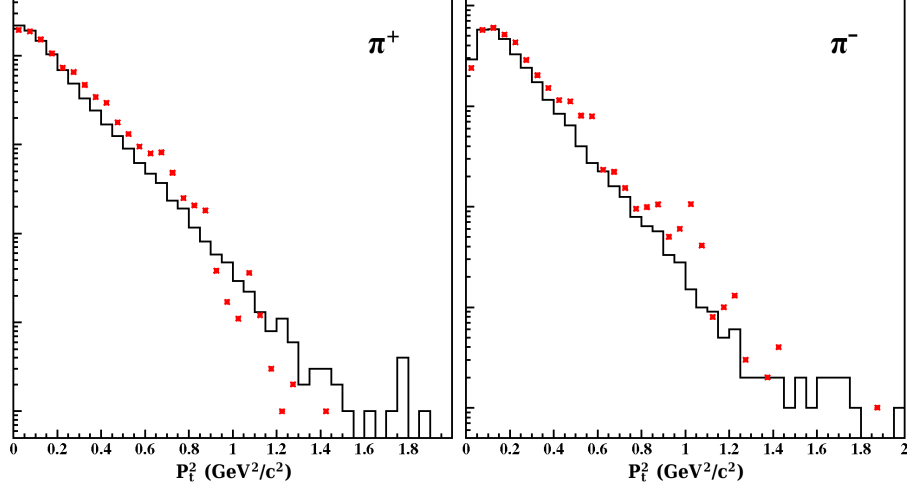


Figure 19: Comparisons, for p_{\perp}^2 (GeV^2/c^2) of charged pions, of the distributions from simulated (red crosses) and experimental (histogram) data using deuterium target.

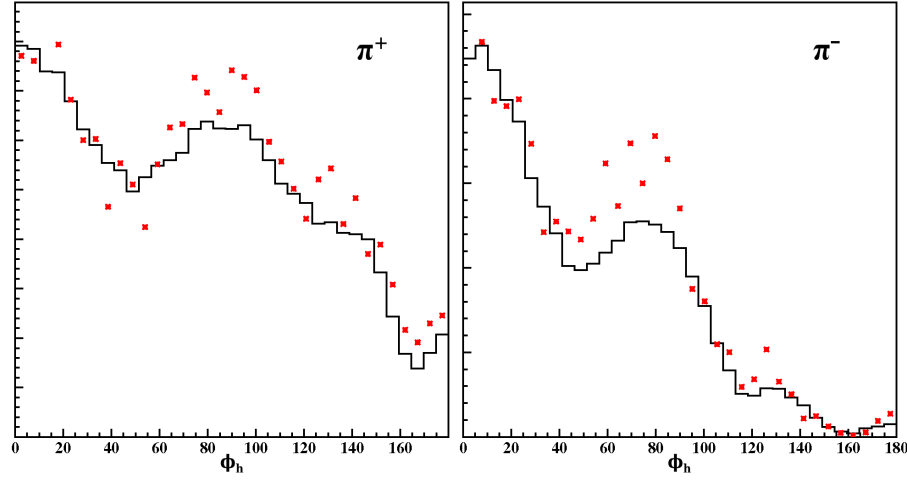


Figure 20: Comparisons, for ϕ_h of charged pions, of the distributions from simulated (red crosses) and experimental (histogram) data using deuterium target.

we used the two different binning presented in table 4. The total number of bins is constrained by the amount of generated data, and must be maintained reasonably low in order to keep a good statistical precision and a manageable bin migration.

Variable	Number of bins	Variable	Number of bins
ν	5	Q^2	5
x_{Bj}	5	ν	5
p_h	7	z_h	7
t	7	t	7
Total	1225	Total	1225

Table 4: Variables and their associated number of bins used on the multi-dimensional binning of our acceptance correction. The left panel shows the variables used on this correction, and the right panel contains the variables used on the evaluation of the related systematic uncertainties.

The weights ($\omega_{\pi^\pm}(\nu, x_{Bj}, p_h, t)$) are then extracted from the simulation using equation 12. However, it turned out that these coefficients should not be applied to data before resolving the issue of the problematic bins that have either

- too large weight values, i.e., very small acceptance, or
- very few reconstructed events leading to large statistical errors, or
- a large fraction of events originally generated in an other bin (bin migration issue).

To eliminate these bins we apply the following cuts:

$$\left(\frac{\delta\omega}{\omega}\right)^2 \times R_c \times \omega < 2, \quad (13)$$

and

$$N_{rec} > 4, \quad (14)$$

where $\delta\omega/\omega$ is the relative error on the weight, and R_c is the proportion of reconstructed events initially generated in an other kinematical bin. Figure 21 shows ω distributions after applying these cuts. Around 900 bins remain for both targets, but we noticed that these weights are much larger for π^- compared to π^+ , as an indication of a larger correction for the inbent particles. In order to maximize the acceptance and reduce the sensitivity to our arbitrary weights' cuts, we corrected the data with an additional two dimensional reweighting factor as:

$$\text{Acc}_2(\nu, p_h) = \frac{\sum_{rec} \omega(\nu, x_{Bj}, p_h, t)}{N_{gen}(\nu, p_h)}. \quad (15)$$

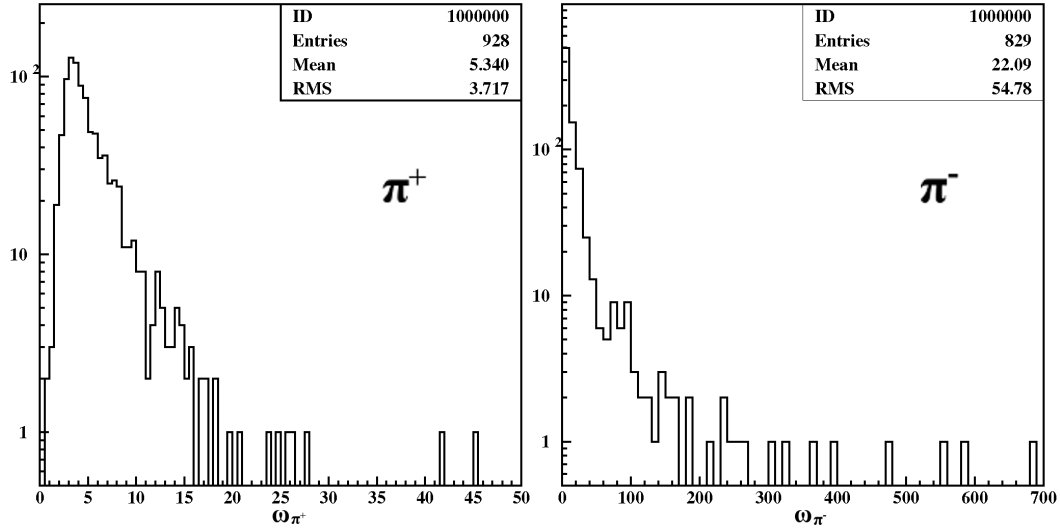


Figure 21: The extracted acceptance correction weights for pions on a deuterium target (not re-weighted).

where ω is the previously calculated weight of either one remaining bin or a bin that was excluded by the cuts. One of the criteria for setting the limits in equation 13 and 14 is to keep reweighting factors, $\omega_2 = 1/\text{Acc}_2$, at the level of a few percents.

In order to correct the number of electrons in multiplicity ratios, we followed the semi-inclusive acceptance correction method by using only the two first dimensions (ν and Q^2). However, the reweighting was not used for electrons as all non-empty bins pass the two cuts, 13 and 14.

Figure 22, where only statistical errors are represented, shows the new results after applying the acceptance correction. The acceptance correction effects appear to be in the order of 10% for multiplicity ratios and 30% for the transverse momentum broadening. This is a surprisingly significant correction with regard to a few centimeters separating the two targets. The reason for such a large correction is that the small shift in the z -vertex position changes slightly the minimum angle of the detector in the region where most hadron production is concentrated, *i.e.* at low p_\perp^2 close to the beam line. The π^- s were more affected due to the inbending magnetic field. Indeed, the low p_\perp^2 π^- s had very low acceptance which led to large correction factors. The large spread in weights makes the errors on $\Delta\langle p_\perp^2 \rangle$ very large, and the related results difficult to exploit. However, our transverse momentum broadening results of both pions matched each other after this correction, which is consistent with HERMES results.

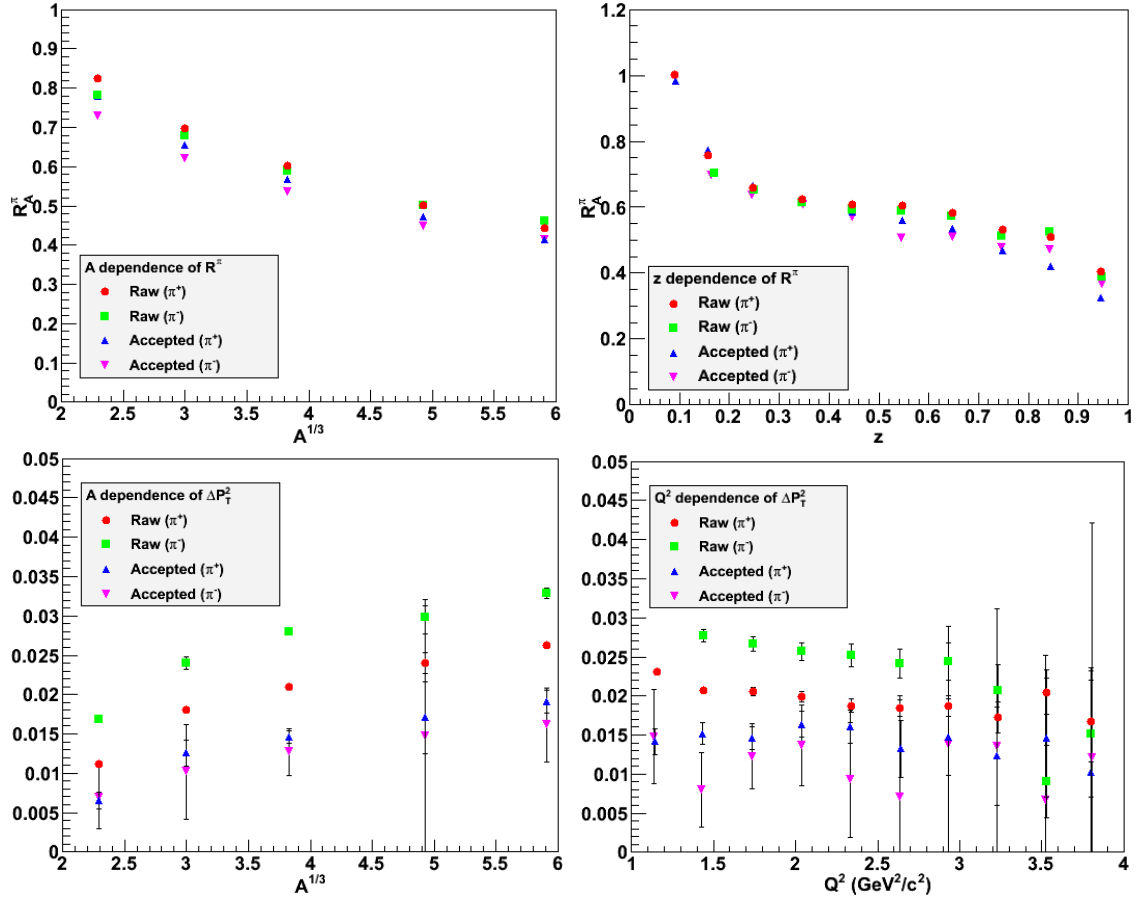


Figure 22: Preliminary results are compared with the acceptance corrected ones, for multiplicity ratios (top) and transverse momentum broadening (bottom). Only statistical errors are shown.

2.4.2 Coulomb Correction

The large electric charge of our nuclear targets create an electric field that should be taken into account at our energies. Besides the fact that the nuclear electric field accelerates or decelerates the incoming and outgoing charged particles, it has some non trivial effects such as the focusing of low energy particles. Aste *et al.* [21] showed that these Coulomb effects could be corrected for by using an effective momentum approximation at large momenta (*i.e.*, $Q^2 > .5 \text{ GeV}^2$). As our kinematics coverage is beyond this limit, we decided to use this approximation on the coulomb correction of our data-sets. According to Aste *et al.*, the best effective potential approximation is given by $\bar{V} = 0.8V_0$, where V_0 is the electrostatic potential at the center of nuclei. The latter is evaluated as $V_0 = -3\alpha_{EM}Z/(2R)$, where α_{EM} is the fine-structure constant, Z is the proton number, and R is the radius of nuclei. Table 5 contains the used values of V_0 and \bar{V} on different nuclear target's analysis. We must note that this Coulomb correction has been applied to both electrons and charged pions before calculating any kinematical variables.

Nucleus	V_0 (MeV)	\bar{V} (MeV)
^2H	-1	-1
C	-4	-3
Al	-7	-6
Fe	-11	-9
Sn	-17	-14
Pb	-23	-19

Table 5: The V_0 and \bar{V} values used on Coulomb corrections for different charged particles.

2.4.3 Radiative Correction

Despite its lower magnitude compared to the strong force, the electromagnetic force may have a non negligible impact on our results. The reason is that even a moderate energy photon emission can modify significantly the measured kinematical variables. To correct this effect, several simulation codes exist [22], however, none of them treat directly the SIDIS production on nuclei. For that reason, a dedicated Monte-Carlo simulation based on existing codes was developed.

Simulation The inclusive radiative effects are generated using the RADGEN code [23], which includes Feynman diagrams shown in figure 23. Using this code one can evaluate the correction factors for inclusive measurements as $\delta = \sigma_{obs}/\sigma_{Born}$, where σ_{obs} is the measured inclusive cross section, and σ_{Born} is the Born cross section. As

RADGEN is also a Monte-Carlo generator for photon emissions, it could be used to modify the virtual photon kinematics before the hadron production in any DIS generator. This allows the evaluation of the radiative effects on semi-inclusive measurements by implementing RADGEN inside the main Monte-Carlo event generator.

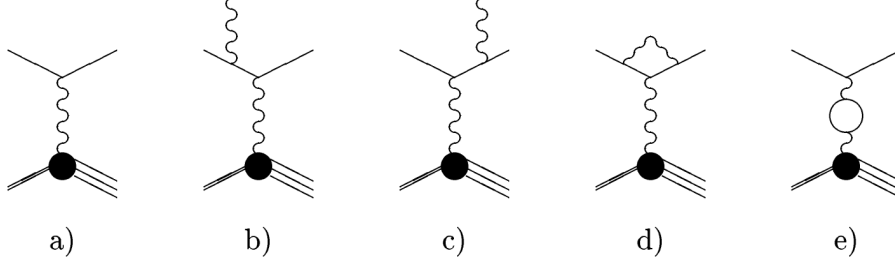


Figure 23: Diagrams taken into account in RADGEN [23]. The diagrams b) to e) contribute to the first order calculation of the radiative effects on Born cross section (diagram a)).

The Monte-Carlo simulation was done using the event generator, GENIE [24], that describes well electron-nucleus interactions. Indeed, GENIE contains the quasi-elastic scattering⁷, which is considered as the main channel generating radiative events in the DIS region [25]. This generator includes also hadronic cascades in nuclei, at which pions might be generated in quasi-elastic events. This is an important feature because the quasi-elastic production can not contribute directly to semi-inclusive measurements.

Correction of the Data We generated 100 million events with and without radiative effects for each target. The RADGEN code gave us the magnitude of inclusive correction coefficients, however, the comparison between the two data sets allows the extraction of semi-inclusive correction factors.

The ratio of inclusive correction factors, as depicted in figure 24, is relatively small (couple of percents at most) except for low x_{Bj} and high ν . Similarly for the semi-inclusive factors' ratio shown in figure 25 as a function of z and p_{\perp}^2 . However, the associated statistical errors are quite large because only a small fraction of the events involved a photon radiation.

The semi-inclusive part of the radiative correction turned out to be limited in amplitude for the most kinematics, except for high z and p_{\perp}^2 . Thus, we decided to not apply this correction before further studies.

We found a better way to implement the radiative correction, that is not limited by the used MC technique. We will implement it in the second version of the note as we do not want to delay the review process because this correction that we already found to be small. Sorry about that.

⁷Elastic scattering off a single nucleon on nuclei.

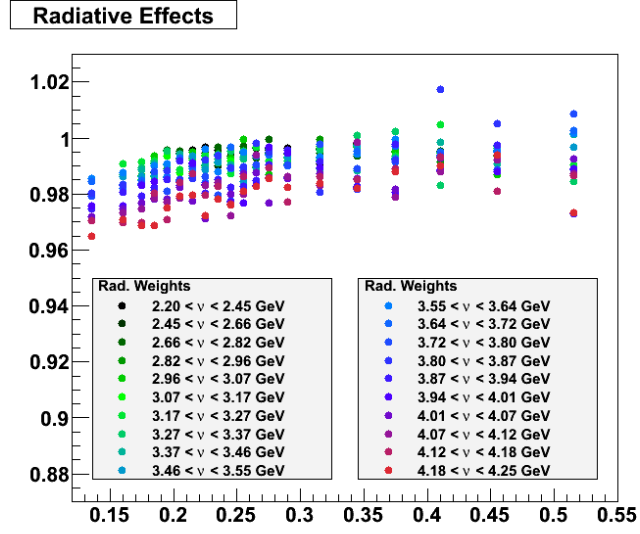


Figure 24: Ratios of radiative correction factors, $\delta_{\text{Pb}}/\delta_{2\text{H}}$, as a function of x_{Bj} in various ν bins.

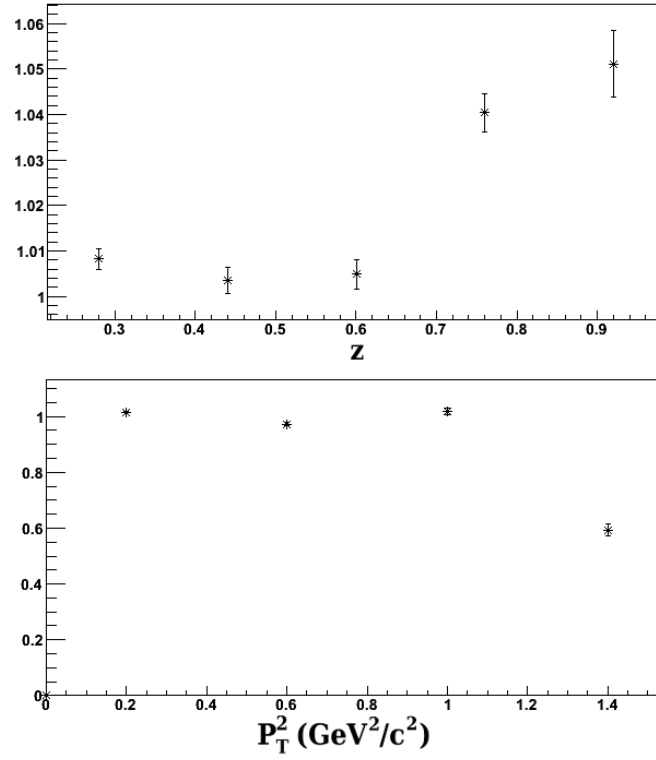


Figure 25: Ratios of radiative correction factors, $\delta_{\text{Pb}}/\delta_{2\text{H}}$, as a function of z (top) and p_T^2 (bottom).

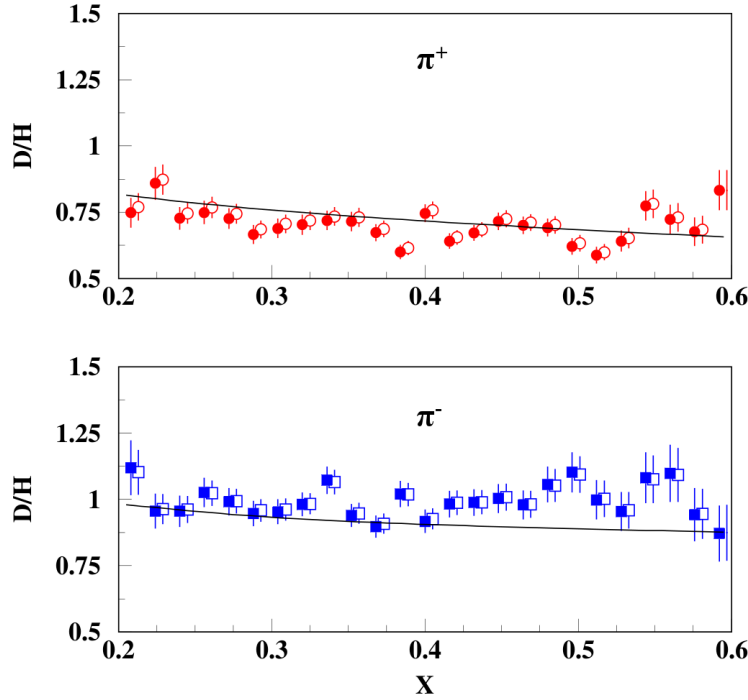


Figure 26: Ratios of deuteron over proton for π^+ s (top) and π^- s (bottom) as a function of x_{Bj} at $z = 0.55$ [26].

2.4.4 Isospin Correction

The important excess of neutrons in heavy nuclei leads to a modification of both π multiplicities on DIS events. Using Hall C results [26], shown in figure 26, we evaluated the correction factors for this effect. Our simple estimation is solely based on proton and neutron numbers that gave π^+ s results shown in table 6. As the effect on π^- s was found to be consistent with zero, no correction was applied to their multiplicity ratios. We attribute a 10% normalization error to the effect of the isospin correction on our results. It is relatively chosen based on the precision of the Hall C measurement, and the limited phase space coverage of Hall-C data compared to ours.

It is important to mention that the isospin correction is applied only to rates, which means applied only to π^+ s multiplicity ratios. The transverse momentum broadening could, in principle, be affected, however, the results from [26] showed no isospin effects in p_\perp^2 . Therefore, we are confident that our $\Delta\langle p_\perp^2 \rangle$ results should not be sensitive to any isospin effects.

We finally note that the A dependence of multiplicity ratios of both charged pions became parallel after the isospin correction⁸ (see figure 27). Considering previous

⁸Within normalization errors presented in section 2.5

Target	Isospin correction
C	0
Al	1.5%
Fe	3%
Sn	8%
Pb	10%

Table 6: Isospin correction applied to π^+ multiplicity ratios for different targets.

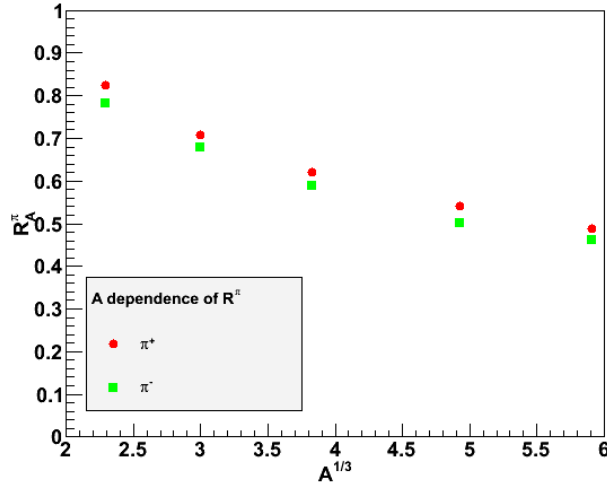


Figure 27: Multiplicity ratios as a function of $A^{1/3}$ with only the isospin correction applied.

measurements and existing models, this result was expected and demonstrated the importance of this correction.

2.5 Systematic Uncertainties

In this section, we are presenting details of our two types of systematic uncertainties. The point-to-point systematic errors, that vary with kinematical variables, were calculated bin by bin for each result. They are caused by uncertainties on the particles' identification cuts and the CLAS acceptance. The normalization errors are attributed globally since they don't depend on kinematics. They are due to acceptance effects, target's misidentification, and the isospin correction.

2.5.1 Quality of the Detection

The simulation of the CLAS detector, using the GSIM package, is used to evaluate the systematic errors correlated with:

- experimental resolution of kinematical variables,
- particles' misidentification,
- particles' re-scattering in different detectors,
- particles' energy loss.

To evaluate those errors, we are comparing the kinematics of reconstructed particles with the generated ones. Each reconstructed particle is associated with its generated parent if both particles have a similar momentum and angle coverage. However, the precision of the measured kinematical distribution Δp , $\Delta\theta$ and $\Delta\phi$ were determined as $\Delta x = \frac{\sum_n |x_{gen} - x_{rec}|}{n}$, where n is the kinematical bin number. Using the same simulation as for the acceptance, we found $\frac{\delta p}{p} = 0.03$, $\delta\theta = 3$ mrad and $\delta\phi = 10$ mrad. Nevertheless of being much larger than the nominal CLAS resolutions published in [27], they are still reasonable for our measurement. Although, we evaluated the systematic errors associated with other variables⁹, such as $\delta Q^2 \sim 0.013$ GeV²/c², $\delta z \sim 0.4\%$, and $\delta P_{\perp}^2 \sim 0.004$ GeV²/c². These errors are overall negligible since they are several times smaller than our usual bin sizes (see figures in a section 2.3.2).

We also evaluated the particles' misidentification and the re-scattering effect in different detectors or coils. The misidentification usually leads to a high contamination on the kinematical distributions tails, which is manifested most in our case on the tail of the p_{\perp}^2 distribution. This effect is due to a low probability to produce high p_{\perp}^2 events, therefore the contribution from the accidental background is relatively increased. As a consequence, we used the following cut $p_{\perp}^2 < 2.5$ GeV²/c², which basically discarded only a very little amount of data (about one π from 30000 pions). The misidentification of electrons was found to be too small in the order of 1 e^- each 1000 events, hence does not contribute significantly to this uncertainty. For pions, the main contamination comes from kaons with momenta above 2 GeV/c ($\sim 3\%$ for π^+ s and $\sim 0.5\%$ for π^- s). Protons also contaminates a π^+ sample at high momenta (up to a few %).

In conclusion, the uncertainty related to particles' misidentification is taken into account in the point-to-point systematic errors by assuming a 100% contamination level. Other effects were found negligible.

2.5.2 Target Reconstruction

Because of some reconstruction errors or a re-scattering on detectors' materials, it is possible to associate a particle with the wrong target. To estimate this effect, we

⁹These values were evaluated for a typical kinematics range. However, the results can be much larger at extreme kinematics (large p_{\perp}^2 or Q^2).

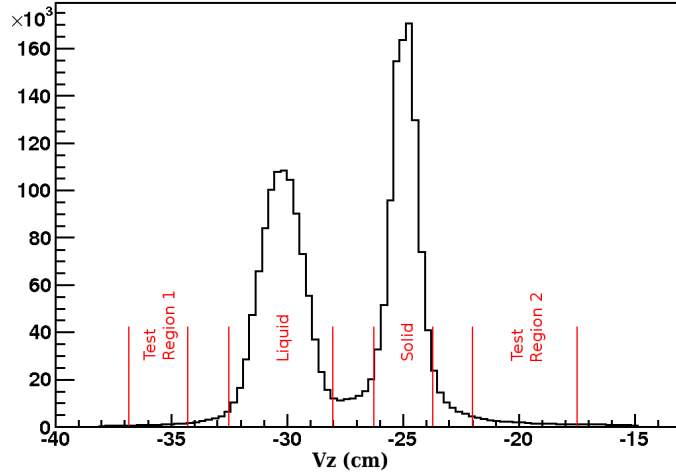


Figure 28: Vertex distribution along a z direction (in cm), i.e. along the beam line. In red are shown the cuts used to evaluate the leak from one target to another.

looked, in the experimental data, at the number of reconstructed events upstream and downstream our targets, where nothing should be detected. Thus, we defined two test regions (see figure 28) to evaluate a targets' contamination. The upstream region, named as a test region 1, was given the size of the solid target's selection cut to evaluate the contamination from the liquid target. However, the downstream region, named as a test region 2, covered the same size of the liquid target's selection cut to estimate the leak from the solid target. The distance between detection and test regions is identical to the distance between the two targets' detection regions.

We found that the number of electrons in the test region 1 and 2 represents, respectively, 1 and 2% of the total number of events. However, in the case of semi-inclusive measurements, where we request two particles in the final state, this number drastically dropped, and became in the order of 0.01%. In conclusion, only the number of electrons is significantly affected by a target's contamination issue, which leads to a normalization error of 1% in all multiplicity ratios.

2.5.3 Acceptance

After testing several different acceptance correction methods, we finally converged with the one using the two different binning presented on a table 4. The difference between these methods gave us an idea about the systematic error associated with this correction. Using our results on iron, we found the relative uncertainties presented in a table 7. We noticed the significantly large errors for π^- s, which were expected, due to their low acceptance and larger weights. Although, systematical errors are considerably large on $\Delta\langle p_{\perp}^2 \rangle$ measurements. This is mainly due to the nature of the $\Delta\langle p_{\perp}^2 \rangle$ observable; as a difference, it would indeed enhance relative errors signif-

icantly. As it was shown in figure 22, error bars became much larger for the corrected $\Delta\langle p_{\perp}^2 \rangle$ from the acceptance effect. This fact indicated an important statistical sensitivity introduced by our weighting methods. The errors on $\Delta\langle p_{\perp}^2 \rangle$ are of the same order, or smaller, than the differences observed between the two weighted data-sets. This is an indication that the uncertainties reported in table 7 are, in nature, similar to the statistical errors, in the sense that both originate from the large variation between event-by-event weights. For this reason, we decided to do not include this error in our systematic budget to avoid double counting this effect.

Variable	Normalization errors	Point to point errors
$R_A^{\pi^+}$	1.2%	1.5%
$R_A^{\pi^-}$	2.5%	2.6%
$\langle \Delta P_{\perp}^2 \rangle_A^{\pi^+}$	5%	11%
$\langle \Delta P_{\perp}^2 \rangle_A^{\pi^-}$	5%	21%

Table 7: Relative errors on pions' observables using the two weighting methods described in the text.

2.5.4 Total Systematic Budget

The point-to-point errors include contributions from a detection contamination and acceptance effects. However, the normalization errors, which are independent of kinematical variables and due to acceptance effects, a target's misidentification and the isospin correction, are summarized in a table 8.

	$R_A^{\pi^+}$	$R_A^{\pi^-}$	$\Delta\langle p_{\perp}^2 \rangle^{\pi^+}$	$\Delta\langle p_{\perp}^2 \rangle^{\pi^-}$
Acceptance	1.2%	2.5%	5%	5%
Target id.	1%	1%	1%	1%
Isospin (Pb)	1%	1%	1%	1%
Total	1.9%	2.9%	5.2%	5.2%

Table 8: Total normalization uncertainties for both charged pions.

3 Results and Discussions

The results presented in this chapter are a selection of the observables that we want to use in the first publication, eventually a long paper will include results as function of all variables. All results were extracted with the following DIS selection cuts: $Q^2 > 1 \text{ GeV}^2/\text{c}^2$, $W > 2 \text{ GeV}$ and $y < 0.85$. To ensure that a factorization holds, we are selecting events with $0.4 < z < 0.7$ ¹⁰ based on the previously published results from [26]. Moreover, this cut also ensures that we are measuring the leading hadron, and avoiding the high z region, which might be contaminated by the decay products of the diffractive production of ρ^0 . Finally, we are applying a cut on $x_F > 0$ to select the forward fragmentation region.

3.1 Multiplicity Ratio

3.1.1 A Dependence

Figure 29 contains our results for the $A^{1/3}$ dependence of the multiplicity ratio. One can see a 5% normalization difference between both pions. However, this difference is not significant as it represents only 1.5 standard deviation of our normalization uncertainty (see table 8).

The attenuation, presented in the figure 29, is not linear neither for $A^{1/3}$ nor $A^{2/3}$. The HERMES data have already showed some indication of this feature [13, 15], but here, the non-linearity, which has important implication on models, is clear. Indeed, it seems difficult to conciliate the prehadron absorption models with this result. Prehadrons are expected to have their cross sections increasing with time and, therefore, distance. On the parton energy loss side, the BDMPS calculation gives a parton energy loss proportional to $L^2 \propto A^{2/3}$, which is in contradiction with this result. However, this statement does not hold at low energy, and might be modified if the production time occurs inside the nuclei.

3.1.2 Cronin Effect

The Cronin effect is characterized by a large increase of the multiplicity ratio at high p_{\perp}^2 ($\sim 1 \text{ GeV}^2/\text{c}^2$), which is a controversial result in hadronization studies. Indeed, whereas SLAC measurements [8] did not show such an effect, HERMES [13] measured a significant increase of the multiplicity ratio with p_{\perp}^2 . Our result (figure 30 (left)), integrated over all other variables, showed a pattern similar to the HERMES measurement. However, there are some potential contributions from the target fragmentation and the Fermi motion.

¹⁰This cut is not applied for plots with results as a function of z .

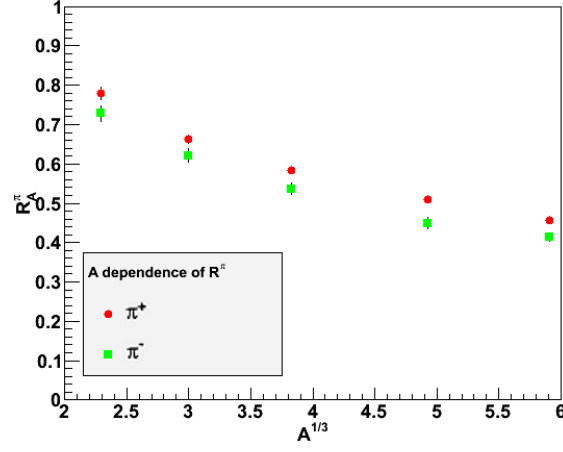


Figure 29: $A^{1/3}$ dependence of the multiplicity ratio. Normalization uncertainties are not shown.

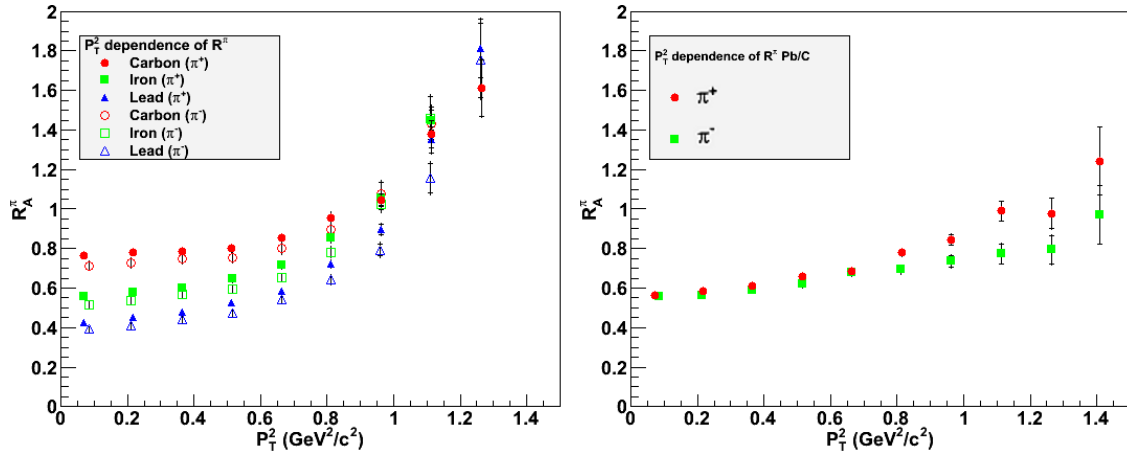


Figure 30: Multiplicity ratios as a function of p_{\perp}^2 (GeV^2/c^2) for both charged pions. Left: The usual multiplicity ratio results. Right: Lead results normalized to carbon. Normalization uncertainties are not shown.

Fermi motion effects can be significantly reduced by modifying our regular observables. Indeed, using carbon for normalization, instead of deuterium, most effects of Fermi motion cancel out. Moreover, acceptance effects (section 2.4.1) will also be mostly canceled in such a ratio, leading to a reduction of their systematic errors dominated mainly by the normalization error. The normalized lead multiplicity ratio to carbon is presented on figure 30 (right). There is an attenuation, at low p_{\perp}^2 , similar to the usual multiplicity ratio of iron. This can be understood based on the difference of both nuclei radii, $R_{Pb} - R_C \sim R_{Fe}$. Nevertheless, the observed enhancement with p_{\perp}^2 is much more modest than in iron. At first sight the difference can be attributed to Fermi motion, which might affect the normalized measurement with deuterium compared to carbon.

In figure 31, the multi-dimensional multiplicity ratio results are presented. HERMES found an important z dependence of the Cronin effect [13, 28]. That can be treated as a sign of an essential contribution from a target fragmentation. The present result (figure 31 (left)) does not show this behavior, which could be due to our strict cut on z ($z > 0.4$ whereas HERMES used $z > 0.2$) that leads to a smaller target fragmentation contamination. The second result, binned in p_{\perp}^2 and ν (figure 31 (right)), showed an important ν dependence of the Cronin effect. However, HERMES results did not exhibit such a ν behavior. This is a clear evidence of the importance of the Fermi motion effect in our measurement.

The result of the lead to carbon multiplicity ratio, figure 30 (right), has another interesting feature: the π^+ s have a stronger Cronin effect. However, the signification of this observation is not clear. This could be a contribution from target fragmentation, as we might expect more positive particles would originate from nuclei than negative ones. This could also come from other sources such as the isospin effect or a factorization breaking at high p_{\perp}^2 . However, no test of these features exists in our kinematical range¹¹. Last but not least, it could be correlated with the hadronic rank and reflect some hadronization properties. Indeed, as we probe mostly valence quarks at our energies, π^+ s are more likely to be the leading hadrons compared to π^- s.

In conclusion, our results indicate that the HERMES results were affected by a target fragmentation and that our results are affected by the Fermi motion. These effects can be easily controlled by a careful selection of our observables. In this regard, the Pb/C ratio seems to give cleaner results than Fe/D.

3.1.3 ν Dependence

The HERMES collaboration clearly observed a rise of the multiplicity ratio with ν from 4 till 22 GeV. However, at first sight to our results (figure 32 (left)), no dependence is observed, besides a slight increase in lead. However, the Fermi motion could cancel most of this hadronization effect, and what left will be washed out with the acceptance

¹¹Results of [26] covered only $p_{\perp}^2 < 0.2 \text{ GeV}^2/c^2$.

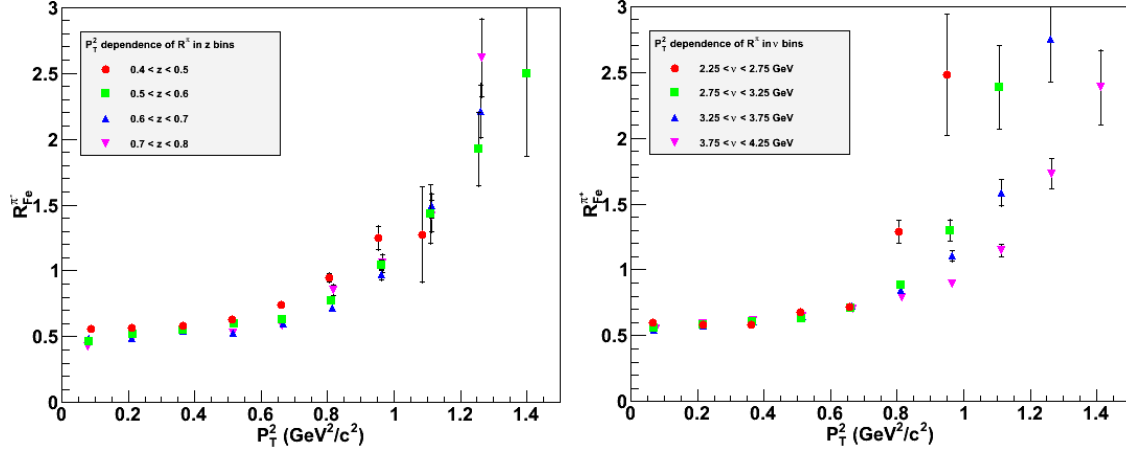


Figure 31: Positive pions multiplicity ratios as a function of p_{\perp}^2 (GeV²/c²) for different z bins (left), and different ν (GeV) bins (right). Normalization uncertainties are not shown.

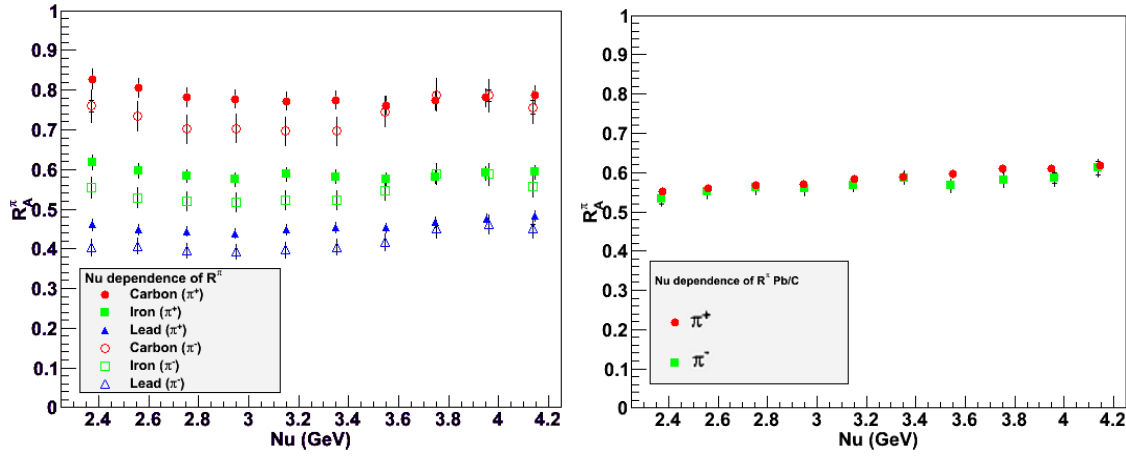


Figure 32: Multiplicity ratios as a function of ν (GeV) for both charged pions. Left: The usual multiplicity ratio results. Right: Lead results normalized to carbon. Normalization uncertainties are not shown.

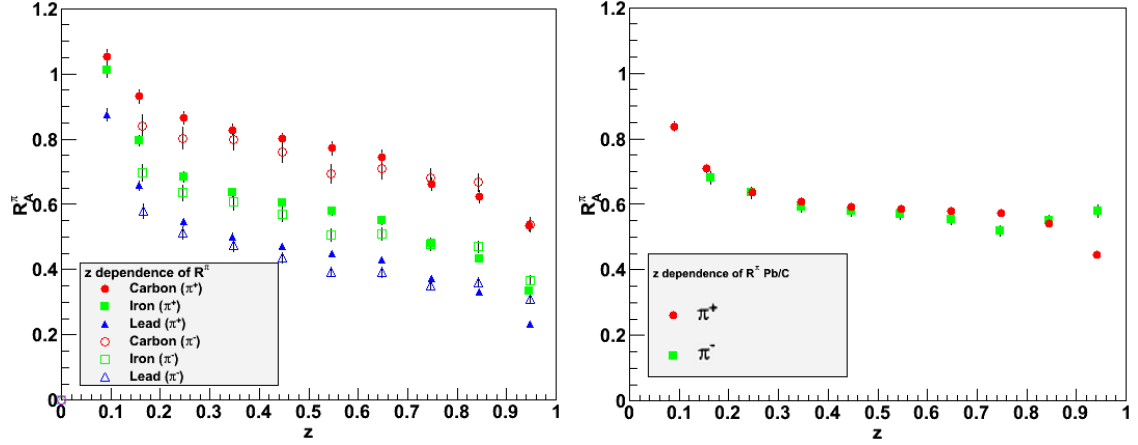


Figure 33: Multiplicity ratios as a function of z for both charged pions. Left: The usual multiplicity ratio results. Right: Lead results normalized to carbon. Normalization uncertainties are not shown.

correction systematic uncertainty. The normalized multiplicity ratio to carbon, however, offers a cleaner result with a slope consistent with what was observed on a much larger range of HERMES data.

We must note the similar behavior of both pions results in a figure 32 (right). This confirms our previous remark that the difference observed in the regular multiplicity ratio might originate from the normalization uncertainty caused by the acceptance correction. Also, there is no clear difference between both charged pions on the integrated multiplicity ratios as a function of ν .

3.1.4 z Dependence

The multiplicity ratio was observed to decrease with z in HERMES data, whereas this behavior was not significant in other experiments. Indeed the nature of this behavior is questionable as the target fragmentation also get reduced with z , hence can mimic the signal. In figure 33 (left), as for HERMES results, we see a clear slope even at values higher than 0.4, where target fragmentation effects are expected to be small. However, the lead to carbon ratio (figure 33 (right)) shows a much flatter behavior in the region of interest (from 0.4 to 0.7). Therefore, this situation seems similar to the Cronin effect, where HERMES observation was enhanced by a target fragmentation. The measurement using the carbon as a basis is, therefore, more useful on isolating effects from the hadronization. However, the low z behavior remains driven by the target fragmentation region. Another strange feature of the data is the behavior at higher z (figure 33 (right)), where the two pions behave differently. However, there is a lack of solid theoretical grounds in this region to interpret this result.

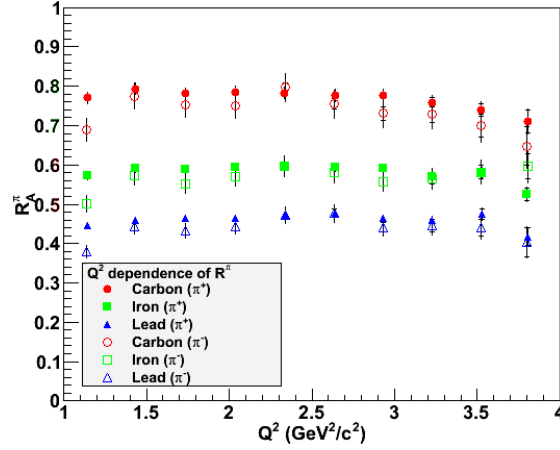


Figure 34: Multiplicity ratios as a function of Q^2 (GeV^2/c^2). Normalization uncertainties are not shown.

3.1.5 Q^2 Dependence

The behavior of hadronization as a function of Q^2 is an important issue, that has direct implications on our understanding of nuclear matter properties in QCD. HERMES results, which covered $1 < Q^2 < 10 \text{ GeV}^2/c^2$, gave a hint of an increase of the multiplicity ratio with Q^2 . Our result, in figure 34, did not indicate any significant Q^2 dependence, hence no conclusions can be made from our measurement.

We can use our large statistics to extract more information by handling the results differently. As a ν dependence is expected for the multiplicity ratio, it might be helpful to use a tighter ν bin to plot the Q^2 dependence (figure 35 (left)), thus remove any coupling between the two variables. As some Fermi motion effects would persist, it is more convenient to show the Q^2 dependence of the normalized multiplicity ratio of lead to carbon, see figure 35 (right). The two results of figure 35 showed a slight increase with Q^2 , but as for HERMES, no evidence is reached on this context. Our leverage on Q^2 appears to be too modest to make a clear measurement.

3.2 Transverse Momentum Broadening

3.2.1 A Dependence

The A dependence of the transverse momentum broadening, presented in figure 36, is a crucial result. The combination of our large statistics with a wide A coverage gave an outright indication of $A^{1/3}$ dependence of $\Delta\langle p_\perp^2 \rangle$. This $\Delta\langle p_\perp^2 \rangle$ effect is found much smaller compared to HERMES measurement[15], which is consistent with theoretical models predicting larger effects at larger energies. However, calculations of the parton energy loss from BDMPs [29] correlated p_\perp^2 with the nuclei radii. A feature

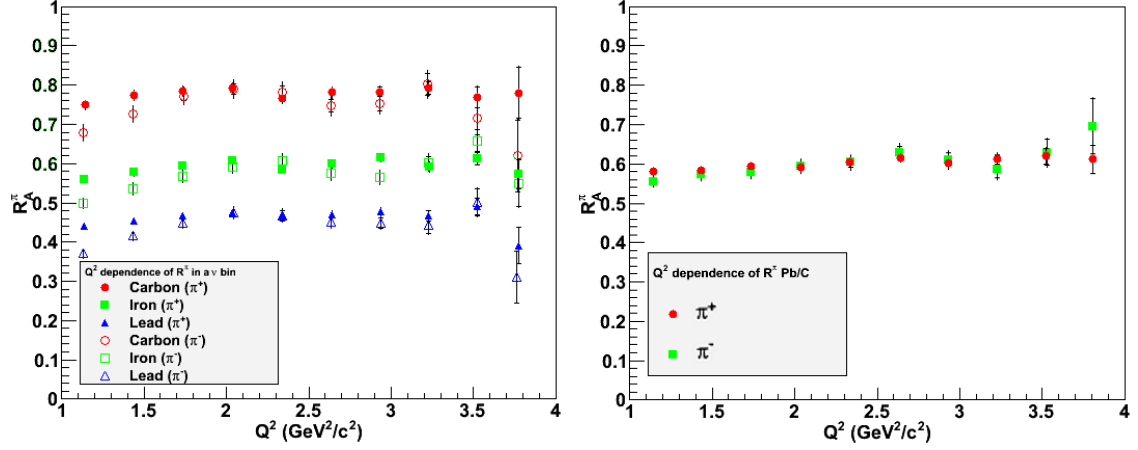


Figure 35: Multiplicity ratios as a function of Q^2 (GeV²/c²) for both charged pions. Left: The multiplicity ratio for a tighter ν bin ($3.25 < \nu < 3.75$ GeV). Right: The normalized multiplicity ratio of lead to carbon. Normalization uncertainties are not shown.

that is not enhanced in our result. Although, by looking to the low energy of our CLAS experiment, one might argue the validity of a direct comparison with BDMPS calculations. Nonetheless, this result shows an unexpected pattern that remains to be explained. One interpretation might favor the occurrence of the production time inside nuclei, as we proposed for the $A^{1/3}$ dependence of multiplicity ratios. In this case, the colored parton would not interact with the whole nuclei which limit the nuclear effect.

3.2.2 Q^2 Dependence

Finally, the Q^2 dependence of $\Delta\langle p_\perp^2 \rangle$ is an important result for the BDMPS based calculation from [30]. They have expected a raise of $\Delta\langle p_\perp^2 \rangle$ with Q^2 , which is not observed in a figure 37. Even a tighter ν bin and a carbon normalization (see figure 38) gave a similar result. In conclusion, within error bars, no effect is observed for $\Delta\langle p_\perp^2 \rangle$ as a function of Q^2 . However, as a theoretical input is missing, it is not clear if we have the needed resolution to observe the effect expected within BDMPS based models.

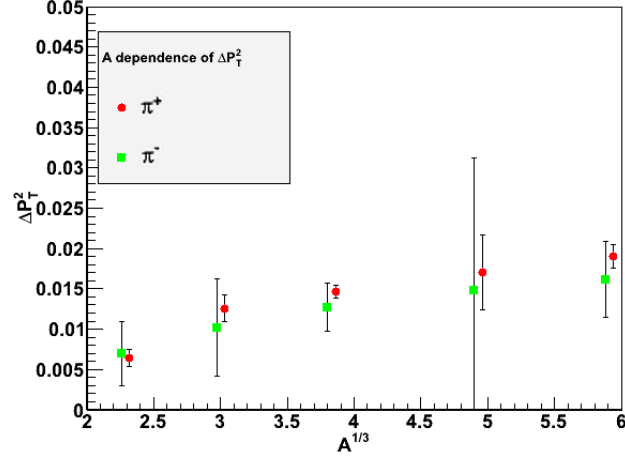


Figure 36: A dependence of $\Delta\langle p_{\perp}^2 \rangle$. Points are slightly shifted for a readability. Normalization uncertainties are not shown.

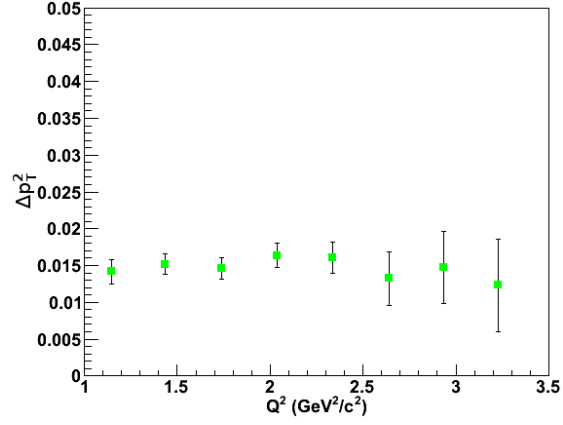


Figure 37: Iron $\Delta\langle p_{\perp}^2 \rangle$ as a function of Q^2 (GeV $^2/c^2$) after applying the regular DIS cuts. Normalization uncertainties are not shown.

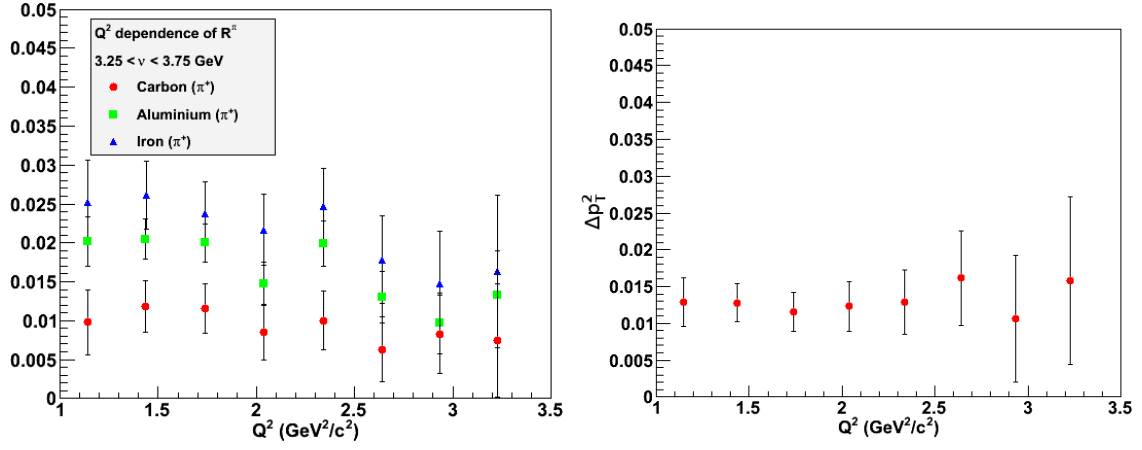


Figure 38: Positive pions $\Delta\langle p_\perp^2 \rangle$ as a function of Q^2 (GeV^2/c^2). Left: The usual observable for a tighter ν bin ($3.25 < \nu < 3.75$ GeV). Right: $\Delta\langle p_\perp^2 \rangle$ of lead relative to carbon. Normalization uncertainties are not shown.

References

- [1] S. Albino, B. A. Kniehl, and G. Kramer, “AKK Update: Improvements from New Theoretical Input and Experimental Data,” *Nucl. Phys.*, vol. B803, pp. 42–104, 2008.
- [2] F. Arleo, “Parton energy loss or nuclear absorption: What quenches hadron spectra at HERA?,” pp. 558–563, 2003.
- [3] B. Kopeliovich, I. Potashnikova, and I. Schmidt, “Measuring the saturation scale in nuclei,” *Phys.Rev.*, vol. C81, p. 035204, 2010.
- [4] K. Gallmeister and U. Mosel, “Time Dependent Hadronization via HERMES and EMC Data Consistency,” *Nucl.Phys.*, vol. A801, pp. 68–79, 2008.
- [5] A. Accardi, F. Arleo, W. K. Brooks, D. D’Enterria, and V. Muccifora, “Parton Propagation and Fragmentation in QCD Matter,” *Riv. Nuovo Cim.*, vol. 32, pp. 439–553, 2010.
- [6] E. Wang and X.-N. Wang, “Jet tomography of dense and nuclear matter,” *Phys.Rev.Lett.*, vol. 89, p. 162301, 2002.
- [7] B. Z. Kopeliovich *et al.*, “Quantum-mechanical description of in-medium fragmentation,” *Phys. Rev.*, vol. C78, p. 055204, 2008.
- [8] L. Osborne, C. Bolon, R. Lanza, D. Luckey, D. Roth, *et al.*, “Electroproduction of hadrons from nuclei,” *Phys.Rev.Lett.*, vol. 40, p. 1624, 1978.
- [9] L. Hand, D. Petersen, H. Scott, K. Gottfried, M. Atac, *et al.*, “Intranuclear cascading in deep inelastic scattering of 150-GeV muons in emulsion,” *Z.Phys.*, vol. C1, pp. 139–142, 1979.
- [10] M. Adams *et al.*, “Nuclear shadowing, diffractive scattering and low momentum protons in μXe interactions at 490-GeV,” *Z.Phys.*, vol. C65, pp. 225–244, 1995.
- [11] A. Arvidson *et al.*, “Hadron production in 200 GeV μ -copper and μ -carbon deep inelastic interactions,” *Nucl.Phys.*, vol. B246, p. 381, 1984.
- [12] J. Ashman *et al.*, “Comparison of forward hadrons produced in muon interactions on nuclear targets and deuterium,” *Z.Phys.*, vol. C52, pp. 1–12, 1991.
- [13] A. Airapetian *et al.*, “Hadronization in semi-inclusive deep-inelastic scattering on nuclei,” *Nucl.Phys.*, vol. B780, pp. 1–27, 2007.
- [14] A. Airapetian *et al.*, “Quark fragmentation to π^\pm , π^0 , K^\pm , p and anti- p in the nuclear environment,” *Phys.Lett.*, vol. B577, pp. 37–46, 2003.

- [15] A. Airapetian *et al.*, “Transverse momentum broadening of hadrons produced in semi-inclusive deep-inelastic scattering on nuclei,” *Phys.Lett.*, vol. B684, pp. 114–118, 2010.
- [16] W. Brooks *et al.*, “Quark Propagation Through Cold QCD Matter,” *A proposal to PAC 22*, 2002.
- [17] K. Hafidi *et al.*, “ Q^2 Dependence of Nuclear Transparency for Incoherent ρ^0 Electroproduction,” *A proposal to PAC 22*, 2002.
- [18] H. Hakobyan, W. Brooks, K. Bruhwel, V. Burkert, T. Carstens, *et al.*, “A double-target system for precision measurements of nuclear medium effects,” *Nucl.Instrum.Meth.*, vol. A592, pp. 218–223, 2008.
- [19] L. El Fassi *et al.*, “Search for the Onset of Color Transparency via ρ^0 Electroproduction off Nuclei,” *Internal Analysis Note*, 2008.
- [20] T. Sjostrand, S. Mrenna, and P. Z. Skands, “PYTHIA 6.4 Physics and Manual,” *JHEP*, vol. 0605, p. 026, 2006.
- [21] A. Aste, C. von Arx, and D. Trautmann, “Coulomb distortion of relativistic electrons in the nuclear electrostatic field,” *Eur. Phys. J.*, vol. A26, pp. 167–178, 2005.
- [22] I. Akushevich, A. Ilyichev, and N. Shumeiko, “Radiative effects in scattering of polarized leptons by polarized nucleons and light nuclei,” 2001.
- [23] I. Akushevich, H. Bottcher, and D. Ryckbosch, “RADGEN 1.0: Monte Carlo generator for radiative events in DIS on polarized and unpolarized targets,” 1998.
- [24] C. Andreopoulos *et al.*, “The GENIE Neutrino Monte Carlo Generator,” *Nucl. Instrum. Meth.*, vol. A614, pp. 87–104, 2010.
- [25] I. Akushevich, A. Ilyichev, and M. Osipenko, “Complete lowest order radiative corrections to five-fold differential cross-section of hadron leptonproduction,” *Phys.Lett.*, vol. B672, pp. 35–44, 2009.
- [26] R. Asaturyan *et al.*, “Semi-Inclusive Charged-Pion Electroproduction off Protons and Deuterons: Cross Sections, Ratios and Access to the Quark-Parton Model at Low Energies,” 2011.
- [27] B. Mecking *et al.*, “The CEBAF Large Acceptance Spectrometer (CLAS),” *Nucl.Instrum.Meth.*, vol. A503, pp. 513–553, 2003.
- [28] A. Airapetian *et al.*, “Multidimensional Study of Hadronization in Nuclei,” *Eur.Phys.J.*, vol. A47, p. 113, 2011.

- [29] R. Baier, Y. L. Dokshitzer, A. H. Mueller, S. Peigne, and D. Schiff, “Radiative energy loss and $p(T)$ -broadening of high energy partons in nuclei,” *Nucl. Phys.*, vol. B484, pp. 265–282, 1997.
- [30] S. Domdey, D. Grunewald, B. Kopeliovich, and H. Pirner, “Transverse Momentum Broadening in Semi-inclusive DIS on Nuclei,” *Nucl. Phys.*, vol. A825, pp. 200–211, 2009.